

Status of LET assessment with active and passive detectors in ion beams

Jeppe Brage Christensen^{a,*}, Iván Domingo Muñoz^{b,c,d}, Pawel Bilski^e, Valeria Conte^f, Pawel Olko^e, Lily Bossin^a, Anne Vestergaard^g, Stefano Agosteo^h, Anatoly Rosenfeldⁱ, Linh Tranⁱ, Željka Knežević^j, Marija Majer^j, Iva Ambrožová^k, Alessio Parisi^l, Tim Gehrke^{d,c,m}, Mária Martišíková^{c,d}, Niels Bassler^{g,n}

^a Department of Radiation Safety and Security, Paul Scherrer Institute, Villigen PSI, Switzerland

^b Department of Physics and Astronomy, University of Heidelberg, Heidelberg, Germany

^c Division of Medical Physics in Radiation Oncology, German Cancer Research Center (DKFZ), Heidelberg, Germany

^d Heidelberg Institute for Radiation Oncology (HIRO) and National Center for Radiation Research in Oncology (NCRO), Heidelberg, Germany

^e Institute of Nuclear Physics Polish Academy of Sciences (IFJ PAN), Kraków, Poland

^f Istituto Nazionale di Fisica Nucleare INFN, Laboratori Nazionali di Legnaro LNL, Legnaro, Italy

^g Danish Centre for Particle Therapy, Aarhus University Hospital, Aarhus, Denmark

^h Energy Department, Politecnico di Milano, and INFN, Sezione di Milano, Milano, Italy

ⁱ Centre for Medical Radiation Physics, University of Wollongong, Wollongong, Australia

^j Ruder Bošković Institute, Radiation Chemistry and Dosimetry Laboratory, Zagreb, Croatia

^k Nuclear Physics Institute of the Czech Academy of Sciences, Řež, Czech Republic

^l Department of Radiation Oncology, Mayo Clinic, Jacksonville, Florida, United States of America

^m Department of Radiation Oncology, Heidelberg University Hospital, Heidelberg, Germany

ⁿ Department of Clinical Medicine, Aarhus University, Aarhus, Denmark

ARTICLE INFO

Keywords:

Linear energy transfer
LET
Particle therapy
Microdosimetry
Luminescence detectors

ABSTRACT

This review explores current experimental methods for determining the radiation quality in ion beams. In this context, radiation quality is commonly evaluated using the averaged linear energy transfer (LET), a metric employed to assess the response of both biological and physical systems. Dose and averaged LET can be experimentally determined with passive detectors through various techniques that have seen recent improvements. Another metric related to the LET is the mean lineal energy, which is measurable using microdosimetric detectors. This review focuses on the available possibilities for evaluating the radiation quality using three microdosimeters (mini-TEPC, Silicon Telescope, and SOI Microplus), three passive luminescence detectors (based on optical, thermo-, and radiophoto-luminescence), three track-based detectors (track-etched detector, Timepix, fluorescent nuclear track detector), and a chemical detector based on alanine. A comparison of detector properties is provided along with an overview of the underlying mechanisms enabling LET assessment or measurements of the mean lineal energy with each detector type. Finally, this review summarizes the current possibilities of LET determination with respect to the needs for quality assurance in particle therapy. Areas for future research and development are suggested.

1. Introduction

As ions travel through matter, they deposit energy along their tracks. Quantifying the local energy deposition around particle tracks has been identified as a fundamental challenge in both radiation physics and radiobiology (Scholz and Kraft, 1996). Whether one examines radiation detectors or biological samples, a particle depositing a large amount of energy over a short distance will yield a distinctly different response compared with a particle depositing the same amount of energy over a larger range (i.e. at a lower ionization density), even if

the dose is the same. In dosimetry, this effect can result in a non-linear response of the detectors at higher ionization density, which generally leads to dose underestimation (Yukihara et al., 2022b). Conversely, in radiobiology, a high ionization density can increase the relative biological effectiveness (RBE) and thus, may be utilized advantageously for particle therapy (Friedrich et al., 2013; Karger et al., 2021).

Developments in these research areas have hinged on accurate descriptions and assessments of the deposition of energy along a particle's track. In response, the concept of LET was first introduced by Zirkle

* Corresponding author.

E-mail address: jeppe.christensen@psi.ch (J.B. Christensen).

<https://doi.org/10.1016/j.radmeas.2024.107252>

Received 15 December 2023; Received in revised form 9 July 2024; Accepted 19 July 2024

Available online 24 July 2024

1350-4487/© 2024 The Author(s). Published by Elsevier Ltd. This is an open access article under the CC BY license (<http://creativecommons.org/licenses/by/4.0/>).

et al. (1951), and formally defined in Report 16 of the ICRU (1970), in an attempt to characterize the local energy deposition along an ion track.

Unrestricted LET is defined as the mean energy dE lost by a particle in a medium due to electronic interactions per unit path-length dx along the particle's trajectory, such as

$$\text{LET} = \frac{dE}{dx}, \quad (1)$$

which equals the electronic stopping power of the particle in the given medium. However, radiation fields typically consist of multiple particles and energies, resulting in an LET spectrum rather than a single LET value. In such cases, averaged quantities, such as the dose-averaged LET, are used as an approximate measure of the radiation quality. This averaged LET is then linked to ionization quenching effects to establish a link between detector response and absorbed dose (Bilski, 2010; Parisi et al., 2019a; Christensen et al., 2023), or radiobiological response (Kanai et al., 1997; Sakama et al., 2012; Rørvik et al., 2018).

The need for accurate LET determinations. The advances in the understanding of RBE have sparked interest in the determination and optimization of the LET distribution, for proton therapy in particular (Mohan, 2022). One example that highlights the need for LET optimizations in radiotherapy treatment planning is the occurrence of necrosis in the brain tissue surrounding the lateral ventricles, which can be LET-related. This is a common side-effect of proton therapy, with reported incidence for glioma patients ranging from 14% to 50% (Bahn et al., 2020; Harrabi et al., 2022; Eulitz et al., 2023). Hence, LET optimization holds the potential to reduce the incidence of necrosis within the treated brain tissue (Bassler et al., 2010; Unkelbach et al., 2016).

While modern particle therapy treatment planning systems (TPSs) now encompass the calculation of averaged LET, the possibilities for quality assurance (QA) of the simulated LET distribution is still at an initial stage. This is because the use of LET optimizations in clinical contexts requires the availability of commercial detectors to validate the TPS through experimental determinations of the radiation quality. At a research level, several studies have aimed at validating simulations of clinically relevant LET distributions through experimental LET determinations (Wagenaar et al., 2020; Parisi et al., 2022b; Petringa et al., 2020; Nakaji et al., 2022; Bobić et al., 2023; Muñoz et al., 2024a). However, the experimental assessment of the averaged LET can be accomplished through a variety of detectors with different properties, which will be discussed herein.

Passive detectors may provide information of LET by utilizing the relationship between detector response and LET, as most — if not all — solid-state detectors eventually will experience a variation of the relative detector efficiency with ionization density. If the dose to a passive detector is known a priori and the LET-response characterized, the LET may simply be derived from the measured dose relative to the deposited dose. Equivalently, the LET may be assessed from dose measurements provided by two detectors with different LET-responses. This approach has been used to determine the averaged LET for decades (Bilski, 2006).

In this review, we focus on detectors and methodologies that do not require a priori dose information. This allows for the assessment of LET independently of the dose, aligning with the contemporary trend in radiation dosimetry toward more direct and intrinsic measurement techniques. Ionization quenching effects are associated with an intrinsic LET-dependence (Andreo et al., 2017) related to high ionization densities in the core of charged particle tracks, and should not be confused with the energy dependence, coming from cavity theory. The latter also depends on LET, but is solely related to translation of dose-to-medium to dose-to-water.

The aim of this review is hence to compare the properties of seven passive and four active types of detectors to determine the radiation quality, and in particular the LET. A status of the current measurement possibilities is provided, along with the steps needed to integrate LET-QA in a clinical setting. While the main focus is on LET determination in therapeutically relevant radiation fields, the given conclusions also partly apply to space dosimetry.

1.1. From LET to lineal energy: Concepts in microdosimetry

The first attempts to experimentally determine and characterize the radiation quality through specific ionization measurements were conducted by Rossi and Rosenzweig (1955). They laid the foundation for a theoretical and experimental framework that aimed to investigate the non-uniform and stochastic nature of energy deposition. The motivation behind this framework was to address the limitations of macroscopic quantities such as absorbed dose and LET when describing the effects of radiation on structures (Rossi, 1959).

The lineal energy y is the most used quantity in microdosimetry, and it is defined as the quotient between the energy imparted ϵ in a microscopic volume of matter by a single energy-deposition event and the mean chord length of that volume \bar{l} as

$$y = \frac{\epsilon}{\bar{l}}, \quad (2)$$

where the unit of measurement for the lineal energy is J/m. However, in the field of microdosimetry, it is more commonly expressed in terms of $\text{keV } \mu\text{m}^{-1}$ in a material, often water. The stochastic nature of the lineal energy motivates the definition of the frequency distribution of lineal energy, denoted $f(y)$. This function represents the probability of observing an event with lineal energy within the range of y to $y + dy$. The expectation value of the frequency distribution of the lineal energy is named the 'frequency-mean lineal energy', and is defined as

$$\bar{y}_F = \int_0^{\infty} y f(y) dy. \quad (3)$$

Similarly, the dose distribution of lineal energy, denoted as $d(y)$, represents the probability that one event deposits a fraction $d(y)$ of the total absorbed dose within the lineal energy range y and $y + dy$. The expectation value of the dose distribution of the lineal energy takes the name of dose-mean lineal energy \bar{y}_D and it is related to \bar{y}_F in Eq. (3) through

$$\bar{y}_D = \int_0^{\infty} y d(y) dy = \frac{\int_0^{\infty} y^2 f(y) dy}{\bar{y}_F}. \quad (4)$$

The dose-mean lineal energy \bar{y}_D can be related to averaged LET as described in Kellerer (1985).

However, the direct measurement of energy depositions in real biological sites at the micrometer scale presents significant challenges, which prompted the adoption of the so-called simulation approach.

The simulation approach: Radiation-sensitive proxies for biological volumes. This approach involves creating virtual representations of biological targets using detector-sensitive volumes (SVs) made of materials other than the biological tissue. The simulation ensures an equivalent energy deposition in both the real and simulated volumes along corresponding trajectories of the ionizing particles. Originally, the idea was to replace the biological target with a larger cavity filled with low-density gas, whose chemical composition simulates tissues at a micrometer scale.

Recent advancements in microdosimetry have seen the development of solid-state microdosimeters (Magrin et al., 2023). Although these detectors have the potential to perform pixelated measurements, they typically have a material density larger than that of tissue. In that case, according to the simulation principle, a sensitive volume of silicon with a thickness of less than $1 \mu\text{m}$ is required to simulate $1 \mu\text{m}$ of biological tissue. The use of gas and solid-state detectors to determine microdosimetric spectra will be described below.

1.2. Monte Carlo simulation of the radiation quality

The use of Monte Carlo particle transport simulation codes to determine the LET or energy spectrum in a point or in a detector is a common method to obtain reference LET-values (Kalholm et al., 2021). The average LET ($\bar{\text{LET}}$) can be determined using Monte Carlo particle transport codes by calculating an averaged quantity derived

from the particles crossing the volume of interest. Although LET may be averaged in numerous ways, the two most common ones remain an averaging with respect to a weighting using the fluence or the dose, \overline{LET}_F and \overline{LET}_D , respectively. A robust and frequently used method to calculate \overline{LET}_F or \overline{LET}_D relies on the so-called *Method C* defined in Cortés-Giraldo and Carabe (2015).

However, the choices of the Monte Carlo code itself as well as energy cutoff and particularly the particle filtering affect the calculated LET averages (Kalholm et al., 2021). In particular, an omission of fragments affect the LET values and may cause e.g. \overline{LET}_D to vary significantly (Grzanka et al., 2018; Kalholm et al., 2021; Muñoz et al., 2024a). Due to its weighting, \overline{LET}_D is more sensitive to the omission of fragments and secondaries than the \overline{LET}_F . This aspect has proven especially challenging in treatment planning validation as, in the present stage of development, the \overline{LET} obtained from TPS simulations often disregards the contributions from fragments. Alternatively, for simple geometries, the radiation quality can be approximated through analytical models (Wilkins and Oelfke, 2003).

Experimental determination of the LET in conjunction with Monte Carlo simulations are therefore crucial for the development and implementation of solid quality assurance in particle therapy.

2. Passive detectors for LET assessment

Passive detectors have been used extensively for dosimetry and LET determinations in medical physics and for space applications (Hayashi et al., 1996; Benton and Benton, 2001; Yukihiro and McKeever, 2006; Christensen et al., 2023; Muñoz et al., 2024b). The most common types of passive detectors used to assess LET are based on stimulated luminescence or single-track analysis of solid-state detectors. In this section, special focus is given to the LET estimation with a single, passive luminescence detector, but the LET determination through the use of two different detectors is also covered. An outlook is made to the use of chemical detectors based on an electron paramagnetic resonance (EPR), such as alanine, for LET assessment with a single detector, although they have seen little use for such purposes in recent years (Malinen, 2014).

2.1. Luminescence detectors

The luminescent materials used for LET assessment may have different modes of stimulation, such as light or heat, but they all have luminescence properties that can be correlated with ionization density, i.e. the LET. (McKeever and Yukihiro, 2011; Yukihiro et al., 2022b). Additionally, the intensity of a single luminescence signal can be related to the absorbed dose in the detector. This enables a simultaneous determination of both dose and LET with some luminescent materials (Vana et al., 1996; Granville et al., 2014a; Miyamoto et al., 2014; Bobić et al., 2023).

Although stimulation and readout techniques vary between different luminescent detectors, the signal generation relies on the same physical principles. Ions passing through a crystalline material can generate electron-hole pairs that become trapped in lattice defects or vacancies. The trapped electrons can be excited by stimulation of the detector with an optical or thermal source, after which they recombine with holes, resulting in the emission of light. If luminescence is triggered by an optical source, it is known as optically stimulated luminescence (OSL), while thermoluminescence (TL) refers to luminescence produced by a heat source. OSL and TL use non-repeatable readout processes, as the trapped electrons are released and recombine during stimulation. In contrast, if a radiation-induced color center in the crystalline insulator is created, the induced fluorescence is referred to as radiophotoluminescence (RPL). In principle, the stable luminescence centers do not disappear after readout of the accumulated data and the signal can be probed multiple times, non-destructively. More details on

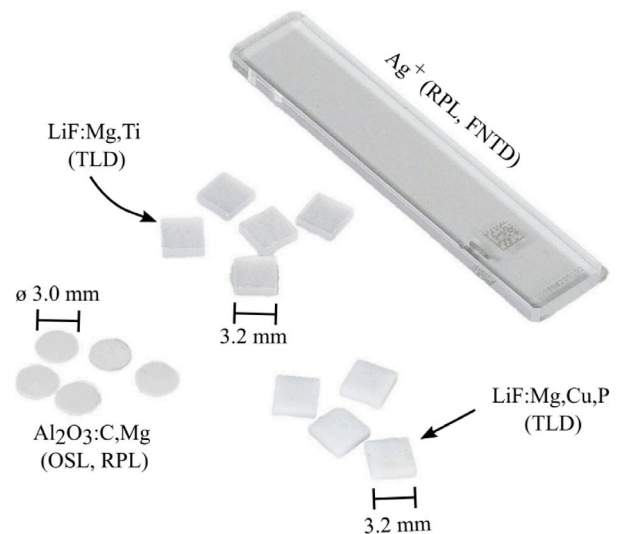


Fig. 1. Examples of four luminescence detector types applicable for LET determination. The LiF:Mg,Ti and LiF:Mg,Cu,P are used as TL detectors. The $Al_2O_3:C,Mg$ disks can be used as OSLDs, FNTDs, and RPLDs. The Ag^+ -activated phosphate glass can be applied as an RPL or FNTD. The detectors can be produced to achieve sizes on the order of millimeters.

the physics behind luminescence detectors can be found in McKeever and Yukihiro (2011).

Most luminescent materials are sensitive to particles relevant to light-ion therapy, but their relative detector efficiency depends on the LET. This change in the detector response as a function of the LET affects the dosimetry, and typically leads to an underestimation of the dose (Bilski, 2010; Christensen et al., 2022). Although the response of luminescence detectors in ion beams has been theoretically modeled using approaches based on microdosimetry (Parisi et al., 2019a; Hirata et al., 2022) or target theory (Edmund et al., 2007), the underlying physical mechanisms are yet to be fully described. However, if the LET can be determined, the ionization quenched dose can be corrected, and the luminescent detectors applied for dosimetry (Bilski, 2006; Christensen et al., 2023). Another advantage of luminescent detectors is their reported dose-rate independence, which enables LET determinations at dose-rates relevant to modern raster-scanning techniques (Christensen et al., 2021; Motta et al., 2023b).

A challenge common to most types of luminescence detectors is the track structure variations of different ions. The relative detector efficiency of luminescent detectors is related to the local ionization density, which depends on the ion type, energy, and material composition. This results in different ions with identical LET producing different detector responses (Sawakuchi et al., 2008). Ultimately, this may challenge the LET determination in mixed particle fields, as the detector response is not uniquely related to an LET value.

Examples of luminescent detectors used for LET measurements covered in this review are shown in Fig. 1. The subsections below outline how each detector type can be used to determine the average LET of the ions traversing the detector.

2.2. Optically stimulated luminescence detectors

Optically stimulated luminescence (OSL) detectors have been applied to personal and space dosimetry for many years (Yukihiro et al., 2006, 2022b). The use of OSL detectors for LET determinations is, however, newer and based on the pulsed stimulation technique detailed in Yukihiro et al. (2006). LET determinations with OSL detectors have been demonstrated in protons (Sawakuchi et al., 2010; Granville et al., 2014a,b, 2016; Christensen et al., 2022) and later in heavier ions (Yukihiro et al., 2015; Christensen et al., 2023).

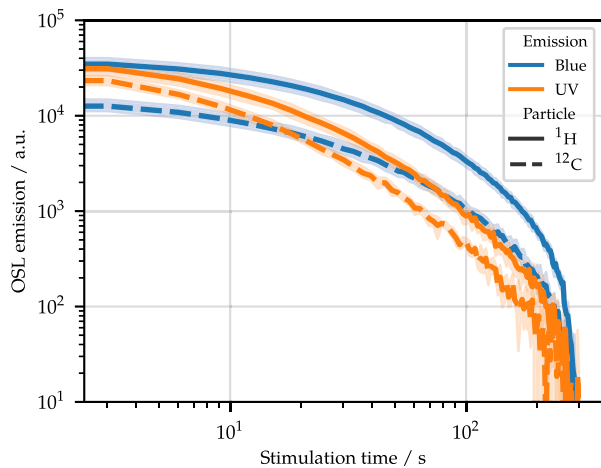


Fig. 2. Example of OSL emissions from two groups of $\text{Al}_2\text{O}_3:\text{C}$ detectors irradiated with 70 MeV/u ^{12}C ions or 230 MeV/u ^1H ions. The dose was 0.25 Gy for all irradiations. The OSL material is associated with two emission bands in the blue and UV parts of the optical spectrum. The lines represent the mean of the OSL signal from five OSL detectors for each of the two radiation qualities, the shaded bands show the standard deviation. The ionization quenching is evident from the relatively lower OSL intensity in the ^{12}C irradiated OSLDs relative to those irradiated in ^1H .

Only two OSL materials have been demonstrated to be applicable for LET determinations in ion beams with a single detector, namely $\text{Al}_2\text{O}_3:\text{C}$ and $\text{Al}_2\text{O}_3:\text{C},\text{Mg}$ (Christensen et al., 2023). Whereas the former material has been used extensively for dosimetry and LET determinations, the latter originally was first used as a fluorescent nuclear track detector (FNTD), see Section 2.5. Both materials, however, rely on the same principles: the materials are characterized by two separate OSL emissions in the blue and UV regions of the optical spectrum, which is attributed to be F and F^+ center emissions, respectively (Yukihara et al., 2006).

The two emission bands can be separated using a spectrometer to detect the signal or, most commonly, by means of a pulsed stimulation technique, where the UV intensity is separated from the blue intensity based on the differences in OSL lifetimes (Yukihara et al., 2006; Christensen et al., 2022). Examples of OSL emission curves of $\text{Al}_2\text{O}_3:\text{C}$ OSLDs following irradiations with ^{12}C and ^1H ions can be seen in Fig. 2.

2.2.1. LET determination with OSLDs

The relative detector efficiency depends on both the ionization density and the OSL material. For comparison, $\text{MgB}_4\text{O}_7:\text{Ce},\text{Li}$ has a linear detector response over the $\overline{\text{LET}}$ values relevant to protons (Yukihara et al., 2022a), whereas both emission bands of the Al_2O_3 -based OSL detectors vary with the $\overline{\text{LET}}$ as illustrated in Fig. 3a. To characterize the OSL response, the detectors were irradiated at quasi mono-energetic ion beams, where the $\overline{\text{LET}}$ in each OSL was obtained through Monte Carlo simulations.

The relative intensity of the UV and blue OSL emission bands from a single OSLD can be used to assess the $\overline{\text{LET}}$ as shown in Fig. 3b. To serve as an $\overline{\text{LET}}$ calibration, a fit to the ^1H , ^4He , and ^{12}C data can be used to relate the ratio of the UV and blue emissions to the $\overline{\text{LET}}$.

Nonetheless, as the relative efficiency for two ions with the same $\overline{\text{LET}}$ differs, the use of a single function to relate the OSL response to $\overline{\text{LET}}$ is merely an approximation (Sawakuchi et al., 2008). It has been demonstrated, that the relative efficiency of different ion types can be better modeled with other radiation quality metrics, e.g. using Q_{eff} (Kaltholm et al., 2022; Christensen et al., 2023). For dosimetry in ion beams with OSLDs, the blue emission band is usually preferred due to its relative efficiency being closer to unity, which reduces the magnitude of the ionization quenching correction factors (Christensen et al., 2022).

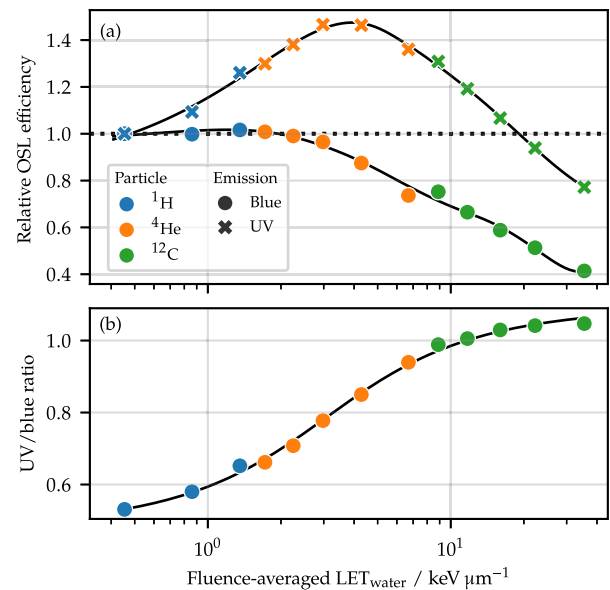


Fig. 3. (a) The relative detector efficiency for both the UV and blue emission bands of $\text{Al}_2\text{O}_3:\text{C}$ detectors irradiated at ions with different $\overline{\text{LET}}$ values. (b) the ratio of the UV intensity to the blue intensity for several $\overline{\text{LET}}$ values. The solid line shows a fit to the data, which can be applied for an LET assessment. The use of a single function to model the response of the different ions is an approximation. Source: Data from Christensen et al. (2023).

2.2.2. OSLD preparation

OSLDs can be prepared from powder mixed with a binder and spread onto a thin plastic substrate to form thin films ($< 100\ \mu\text{m}$ thickness) to minimize the perturbation of the radiation field (Ahmed et al., 2014). The OSLDs can be cut out from the film into any desired shape, where the upper dimension is limited by the OSL reader, typically around 1 cm diameter. Due to their high sensitivity, the OSL detectors may be cut to sub-millimeter disks, effectively serving as point-detectors (Yukihara et al., 2005). To avoid exposure to ambient light bleaching the detector and erasing the OSL signal, the detectors need to be protected from light during and after irradiation, e.g. by being wrapped in opaque tape or placed in a container.

2.2.3. OSLD properties

The point-like size of OSL detectors enable simultaneous dose and $\overline{\text{LET}}$ determination with a negligible perturbation of the radiation field. With the use of a readout sequence with a reference irradiation as described in Yukihara et al. (2005), a reproducibility at a 1%-level can be achieved. Whilst the Al_2O_3 -based OSL detectors enable LET measurements in ^1H , ^4He , and ^{12}C ions shown in Fig. 3b, both materials saturate in oxygen and heavier ions which limits the $\overline{\text{LET}}$ determination capabilities (Yukihara et al., 2015; Christensen et al., 2023). The dose-rate independence of OSLDs (Karsch et al., 2012; Christensen et al., 2021; Motta et al., 2023a) is a key advantage but doses may affect the LET determination through track overlap. This track overlap depends on the radial ionization distribution within an ion track, which varies with the ion type and energy. For protons, the track overlap affects the LET determination above $\approx 1\ \text{Gy}$ at 230 MeV/u, whereas the threshold is above $\approx 10\ \text{Gy}$ in 230 MeV/u ^{12}C ions. The possibility of preparing the OSLDs to point-like sizes enable high-resolution determination of both dose and LET within anthropomorphic phantoms, see Bobić et al. (2024).

2.3. Thermoluminescence detectors

Thermoluminescence (TL) detectors have been applied for dosimetry in space for decades (Hayashi et al., 1996; Vana et al., 1996; Olko

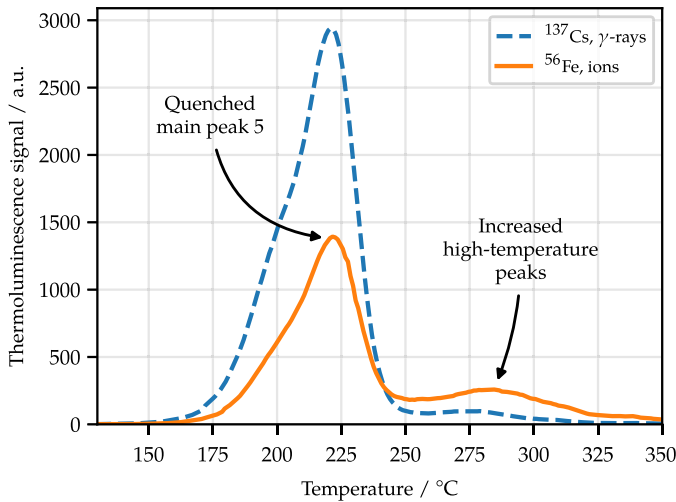


Fig. 4. Comparison of LiF:Mg,Ti thermoluminescence glow curves after exposures to identical doses of iron ions ($300 \text{ keV } \mu\text{m}^{-1}$) and gamma rays. The high-LET ^{56}Fe glow curve shows relatively quenched main TL peak as well as an increased intensity of high-temperature peaks relative to the low-LET ^{137}Cs gamma irradiation. The differences in the glow curves can be related to the LET through Eq. (5).

et al., 2002; Bilski, 2006, 2010; Berger et al., 2013, 2017), and have been used to assess the LET in ion beams (Hajek et al., 2008; Parisi et al., 2019a, 2020). Throughout the years, multiple techniques for determining LET with TL detectors have been suggested. However, they all share a common principle: the thermoluminescent signal is comprised of two components, which exhibit distinct LET dependences. The ratio between these components acts as an indicator for the LET. The two components can be represented by two peaks in the TL glow curve of a single detector, or signals from two different types of TLDs.

2.3.1. LET determination with a single TL detector

Probably the most widespread method consists on utilizing the high-temperature peaks of LiF:Mg,Ti glow curve. This method, named high-temperature ratio (HTR), was developed by Vana et al. (1996). The high-temperature ratio is defined as

$$\text{HTR} = \frac{A_k/I_k}{A_g/I_g}, \quad (5)$$

where A_k and A_g are the integrals of the high-temperature signals, I_k and I_g are the heights of the main peak 5, measured after exposures to the studied radiation (k) and after reference gamma radiation (g) (Berger et al., 2006). The differences can be seen in Fig. 4, where glow curves following irradiation with low-LET ^{137}Cs gamma and high-LET ^{56}Fe ions are shown. The temperature integration region was optimized to (248–310) °C, for a peak 5 set at 220 °C (Berger et al., 2006; Bilski, 2010).

Fig. 5 shows the HTR for LiF:Mg,Ti for multiple ions and $\overline{\text{LET}}$ values. The solid line fitted to the data relates the HTR to the $\overline{\text{LET}}$. Another material proposed for the purpose of LET determination is $\text{CaF}_2:\text{Mg}$ (Hoffmann and Moller, 1980). Its low-temperature TL peak (peak 3) shows an efficiency decreasing with increasing LET, while the efficiency of the well-separated high-temperature peak (peak 5) remains constant over a wide range of LET values (Hajek et al., 2008).

2.3.2. LET determination with two TL detectors

The use of two different TL detectors, namely LiF:Mg,Ti and LiF:Mg,Cu,P, is another method frequently used to determine the LET (Bilski, 2006; Bilski et al., 2016; Parisi et al., 2019a, 2020). Despite their practically identical atomic composition, these detectors exhibit very different TL efficiency dependence on ionization density (Parisi

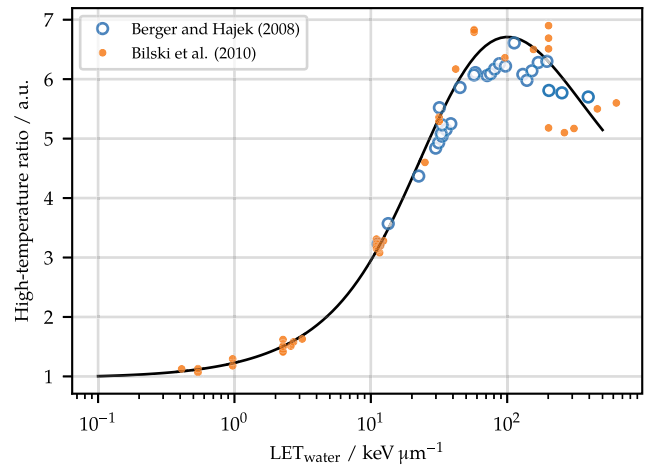


Fig. 5. High-temperature ratio (HTR) for LiF:Mg,Ti detectors as a function of $\overline{\text{LET}}$. The solid line represents the HTR calibration used to assess the LET.

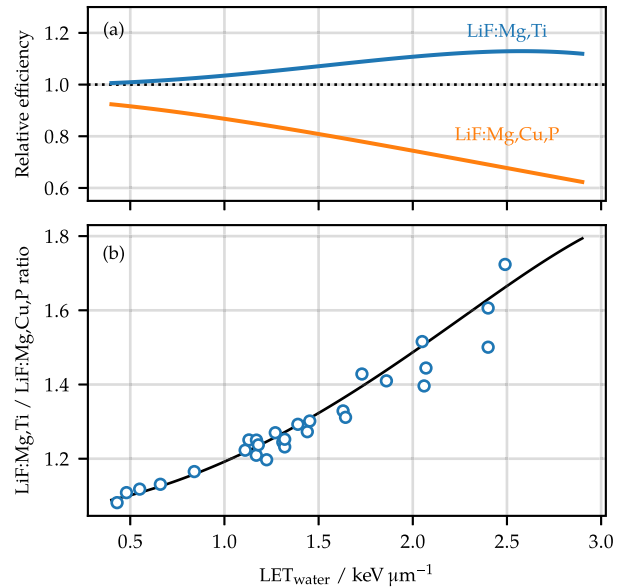


Fig. 6. (a) Relative efficiencies of LiF:Mg,Ti and LiF:Mg,Cu,P as calculated in Olko and Bilski (2021). (b) shows the ratio of the two functions in (a) plotted as a solid line against measurements (markers) acquired in proton beams. Source: Data from Sadel et al. (2015).

et al., 2019b), similar to that of the intensities of the two OSL emission bands in Fig. 3a. The relative efficiency of LiF:Mg,Cu,P is significantly reduced for high-energy protons compared with gamma-rays, as shown in Fig. 6a. In contrast, the relative efficiency of LiF:Mg,Ti starts to quench only for radiation with LET above about $5 \text{ keV } \mu\text{m}^{-1}$, and the decrease in efficiency with LET is much less steep (Olko and Bilski, 2021). Fig. 6b shows the ratio of the two TL detectors as a function of the proton LET for both measurements (markers) and using the ratio of the two calculated detector efficiencies in Fig. 6b.

2.3.3. TL detector preparation

TLDs typically have the shape of square chips or circular pellets with a size of (3–5) mm and a thickness below 1 mm. For special applications, smaller TLDs may be manufactured or used in the form of powder. In contrast to OSLDs, most TLDs can normally be exposed to ambient light. Usually, before use, they should be reset using a specific thermal treatment as outlined in e.g. Yukihiro et al. (2022b). This

makes the TLDs easier to re-use compared to OSLDs, which are difficult to bleach with light.

Although the $\overline{\text{LET}}$ determination with a single TLD presents several advantages, the HTR is strongly affected by the used thermal treatment, which means that a protocol-specific $\overline{\text{LET}}$ calibration is needed. This challenge is generally avoidable when the $\overline{\text{LET}}$ is assessed through the ratio of two detectors.

2.3.4. TL detector properties

Similarly to the OSL detectors presented in Section 2.2, the TL detectors are dose-rate independent but are affected by the effects of track overlap starting at ≈ 1 Gy for protons. The $\overline{\text{LET}}$ determination relying on the HTR in Fig. 5 allows for $\overline{\text{LET}}$ assessment in a range from fast protons below $10 \text{ keV } \mu\text{m}^{-1}$ in water up to $\approx 100 \text{ keV } \mu\text{m}^{-1}$.

2.4. Radiophotoluminescence detectors

Radiophotoluminescent (RPL) materials have been developed over the past decades for applications in personal, environmental, medical, and space dosimetry (Yamamoto, 2011). RPL detectors (RPLDs) have historically been used for dosimetry in sparsely ionizing radiation fields due to their attractive features, which include a high sensitivity and a non-destructive readout. However, in line with other luminescent detectors, the relative RPLD response varies with the local ionization density. This enables a relation to the $\overline{\text{LET}}$ but also causes an ionization quenched response challenging for dosimetry (Chang et al., 2017; Yasui et al., 2021; Sholom and McKeever, 2023; Majer et al., 2023).

The most common RPLD type remains the Ag^+ -activated phosphate glass, which has been used extensively for space dosimetry (Yasuda and Fujitaka, 2000, 2002) and proton dosimetry (Chang et al., 2017; Majer et al., 2023). More recently, $\text{Al}_2\text{O}_3\text{:C:Mg}$ has also been used as an RPLD (Akselrod and Akselrod, 2006; De Saint-Hubert et al., 2021). Whereas $\text{Al}_2\text{O}_3\text{:C:Mg}$ may also be used to assess $\overline{\text{LET}}$ through its OSL signal as described in Section 2.2, Ag^+ -activated phosphate glass also works as a fluorescent nuclear track detector as discussed in Section 2.6. As the distribution of color centers is related to the energy deposition, an RPLD can in principle be used for high-resolution spatial measurements of the radiation field.

2.4.1. LET determination with RPL

RPLDs offer two methods to determine the $\overline{\text{LET}}$. The first one relies on spectral variations with the ionization density, which allows $\overline{\text{LET}}$ assessment using a single detector. The other one exploits the variations of relative detector efficiencies between an RPLD and another detector, similarly to the approach used with TLDs in Section 2.3.2.

2.4.2. LET determination using a single RPL detector

Miyamoto et al. (2014)'s work has demonstrated how a single RPL glass detector may be used to determine the LET. Fig. 7 shows the RPL spectra after irradiation with a 30 kV X-ray tube and alphas from a ^{241}Am source. The intensity of the RPL color center emitting at 2.7 eV ($\sim 460 \text{ nm}$) varies relatively to the color center emitting at 1.9 eV ($\sim 650 \text{ nm}$) between alphas and photon irradiations. This indicates that the ratio of the two peaks can be related to the LET in a similar manner as the HTR approach with TLDs in Fig. 5.

This RPL peak-ratio approach has, however, not yet been applied to determine $\overline{\text{LET}}$ -values, and is subject to several dependencies, in particular the stimulation wavelength and readout temperature (Miyamoto et al., 2014).

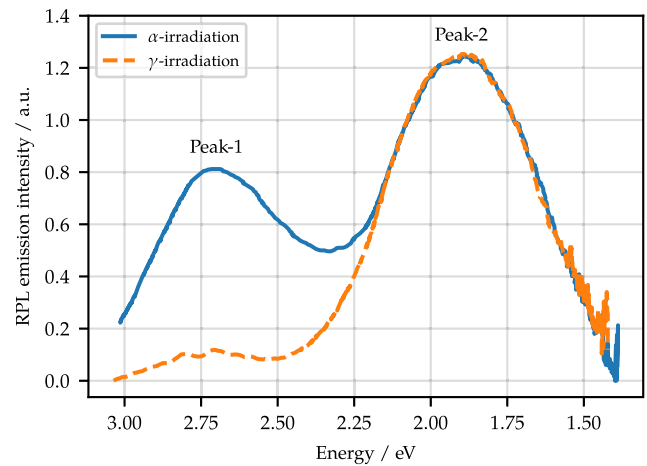


Fig. 7. Relative RPL emission spectra for irradiations with low-LET gamma and high-LET alpha radiation. The ratios of the two emission peaks near 2.7 eV and 1.9 eV can enable an $\overline{\text{LET}}$ determination.

Source: Data from Miyamoto et al. (2014).

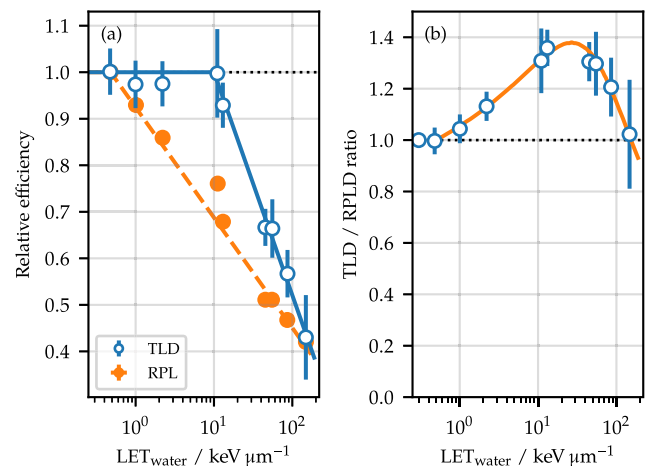


Fig. 8. (a) Relative detector efficiency for the TLD ($\text{Mg}_2\text{SiO}_4\text{:Tb}$) and RPL for several ions and (b) the ratio of the TLD and RPL to be used for an LET determination. The LET in water is analytically derived from the beam energy.

Source: Data from Yasuda and Fujitaka (2000).

2.4.3. LET determination using two detectors

Equivalent to the TLD approach outlined in Section 2.3.2, the different relative detector efficiencies in Fig. 8a allows to establish an LET determination through the characterization of the response between two relative detector efficiencies in Fig. 8b. Similarly, Yasui et al. (2021) related the LET-varying RPL response in a clinically relevant proton beam to that of an ionization chamber to determine ionization quenching corrections. Whilst such an approach enables $\overline{\text{LET}}$ estimations up to $20 \text{ keV } \mu\text{m}^{-1}$ in water, the non-monotonic behavior makes it difficult to apply the approach in mixed fields consisting of particles with LET values both below and above that threshold.

2.4.4. RPL detector preparation

Ag^+ -activated phosphate glass RPLDs can be re-used following a thermal treatment (Yukihara et al., 2022b; Yamamoto, 2011). As $\text{Al}_2\text{O}_3\text{:C:Mg}$ -based RPLDs typically are prepared using plastic films, such a thermal treatment is not feasible. Whereas the glass RPLDs are typically cast as rectangular shapes as shown in Fig. 1, or as $\varnothing 1.5 \text{ mm} \times 12 \text{ mm}$ cylinders, $\text{Al}_2\text{O}_3\text{:C:Mg}$ -based RPLDs can be produced as thin films similar to the OSLDs, thus providing a higher spatial resolution.

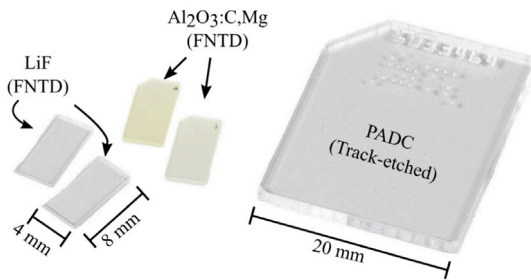


Fig. 9. Fluorescent nuclear track detectors (FNTDs) based on $\text{Al}_2\text{O}_3:\text{C,Mg}$ and LiF along with a track-etched PADC detector.

2.4.5. RPL detector properties

RPLDs' alluring features, such as their insensitivity to ambient light and temperature, coupled with non-destructive readout capability, render them highly appealing for dosimetry applications. This, coupled with the possibility for highly resolved spatial measurements (De Saint-Hubert et al., 2021), means that RPLDs are a good candidate technique for next-generation LET assessments. A recent work by Sholom and McKeever (2023) demonstrated how the RPL emission spectra vary with the dose, in line with Miyamoto et al. (2014)'s work. This may be used to determine the $\overline{\text{LET}}$ in ion tracks, where the high dose in the track core dominates the detector response. However, the use of RPLDs for $\overline{\text{LET}}$ estimation is, to date, limited.

2.5. Solid state track detectors

The field of solid state track detectors emerged in the late 1950s, after Young (1958) discovered that lithium fluoride (LiF) could be used to detect ionizing radiation through visible tracks. The track detector materials relevant to dosimetry and LET assessment are typically based on plastic polymers, glass, and crystals, that are capable of resolving single charged particle tracks. This review focuses on the use of fluorescent nuclear track detectors (FNTDs) and polymer-based track etched detectors (TEDs) for estimation of LET spectra. Whereas the FNTD tracks are made visible through radiophotoluminescence, the TED tracks are chemically etched and observed with an optical microscope.

The most common track detector type, a TED based on polymers, is sensitive to particles above $5 \text{ keV } \mu\text{m}^{-1}$, whereas some crystalline- or glass-based FNTDs can detect particles below $1 \text{ keV } \mu\text{m}^{-1}$ (ICRP, 2013). As the LET and dose determinations rely on single-track analysis, the application of track detectors at clinically relevant fluences is limited due to the track overlapping at doses relevant for particle therapy. For space applications, luminescent and track etched detectors are often used together to map the low-LET and high-LET components, respectively (Vanhavere et al., 2008).

The technology behind FNTDs was initially reported for optical data storage and imaging applications (Akselrod et al., 2003), and was shortly after applied to LET spectroscopy in ion beams (Akselrod and Akselrod, 2006; Sykora et al., 2008; Greilich et al., 2013; Bartz et al., 2014; Klimpki et al., 2016; Muñoz et al., 2024a). Whilst FNTDs mainly have been applied to ion beams, track etched detectors have been used onboard several space missions (Ambrožová et al., 2017; Hayashi et al., 1996), often together with the luminescence detectors described in Section 2.1. Fig. 9 shows FNTDs and track etched detectors, which can be used to measure the LET spectra. The latter can be used to calculate the absorbed dose and LET.

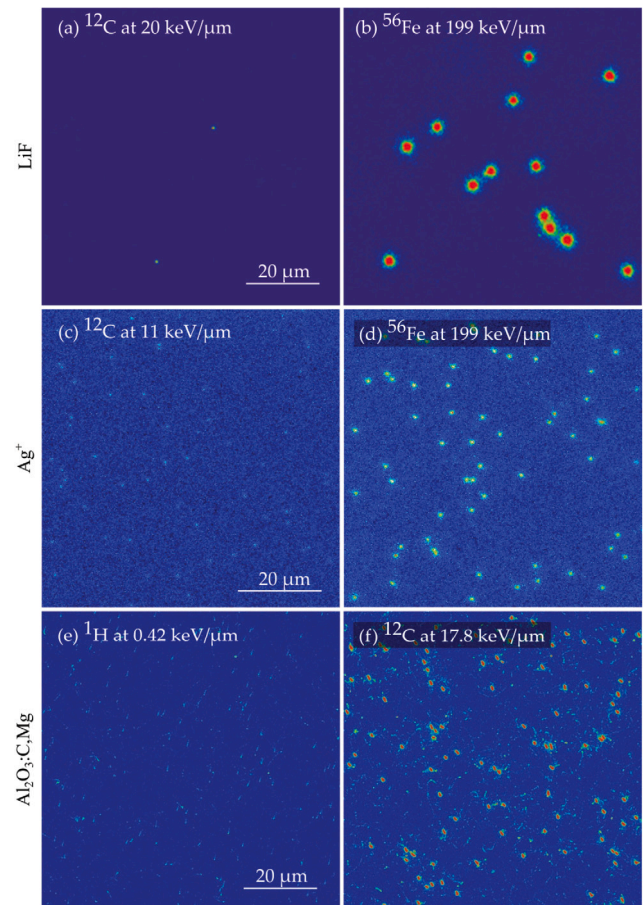


Fig. 10. Fluorescence images of LiF FNTDs irradiated in (a) ^{12}C -ions with a LET of $20 \text{ keV } \mu\text{m}^{-1}$ and (b) ^{56}Fe ions at $199 \text{ keV } \mu\text{m}^{-1}$ in water. Images of Ag^+ -activated phosphate glass FNTDs after irradiations with (c) ^{12}C -ions with a LET of $11 \text{ keV } \mu\text{m}^{-1}$ and (d) ^{56}Fe ions at $199 \text{ keV } \mu\text{m}^{-1}$ in water. Fluorescence images of $\text{Al}_2\text{O}_3:\text{C,Mg}$ irradiated with (e) ^1H ions at $0.42 \text{ keV } \mu\text{m}^{-1}$ and (f) ^{12}C ions at $17.8 \text{ keV } \mu\text{m}^{-1}$. Source: Figures reproduced from Bilski et al. (2019) and Kodaira et al. (2020).

2.6. Fluorescent nuclear track detectors

FNTDs exploit the photoluminescence (PL) phenomenon described in Section 2.1 along with modern microscopy techniques. Whereas the RPLD in Section 2.4 may provide an estimate of LET through variations in the RPL spectrum from the macroscopic detector volume at once, the non-destructive PL signal is here used to visualize the traces left behind single ionizing particles. Due to the relatively small free path of the charge carriers liberated by ionizing particles passing through the FNTD, the transformed color centers are situated close to the ionizing events.

Up to now, three materials have been investigated as FNTDs, namely $\text{Al}_2\text{O}_3:\text{C,Mg}$, un-doped lithium fluoride (LiF), and silver-activated (Ag^+) phosphate glass (Bilski et al., 2018; Kodaira et al., 2020; Sykora et al., 2008). Examples of fluorescence images from LiF, Ag^+ phosphate glass, and $\text{Al}_2\text{O}_3:\text{C,Mg}$ FNTDs irradiated with mono-energetic ions are shown in Fig. 10. The intrinsic sensitivity of each crystal depends primarily on the availability of color centers. However, the detected luminescence intensity also depends on the imaging system and readout parameters.

2.6.1. LET determination with FNTDs

Generally, the number of transformed color centers in a given crystal volume increases with the ionization density and, consequently, the number of fluorescence photons emitted upon stimulation increases

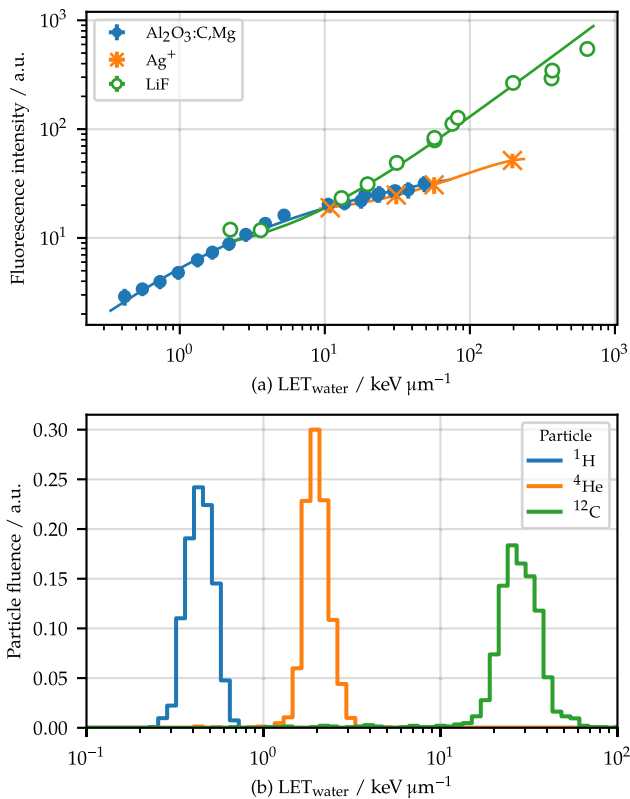


Fig. 11. (a) Fluorescence intensity of $\text{Al}_2\text{O}_3:\text{C,Mg}$ (Muñoz et al., 2022) FNTDs, Ag^+ -activated phosphate glass FNTDs (Kodaira et al., 2020), and LiF FNTDs (Bilski et al., 2019) after irradiation with mono-energetic ions, normalized to the intensity at $10 \text{ keV } \mu\text{m}^{-1}$. The solid lines serve as a calibrations, relating the fluorescence intensity to the LET. (b) Examples of LET spectra determined with $\text{Al}_2\text{O}_3:\text{C,Mg}$ FNTDs. Source: Data from Muñoz et al. (2022).

with the LET (Kodaira et al., 2020; Sykora et al., 2008). Such a relationship allows to calibrate the fluorescence intensity as a function of the LET values, as illustrated in Fig. 11a for $\text{Al}_2\text{O}_3:\text{C,Mg}$, Ag^+ -activated phosphate glass, and LiF . Once the calibration between fluorescence intensity and LET has been established, LET spectra can be calculated on a track-by-track basis, as shown in Fig. 11b for protons, ^4He and ^{12}C ions (Muñoz et al., 2022). It is worth noticing that this approach can also be applied for mixed radiation beams (Verkhovtsev et al., 2019).

For $\text{Al}_2\text{O}_3:\text{C,Mg}$ used as an FNTD, the local saturation — i.e. the depletion of available color centers within the track core and its vicinity — varies with the LET. This is evident from Fig. 11a, where the fluorescence intensity of the track in $\text{Al}_2\text{O}_3:\text{C,Mg}$ becomes less pronounced as the LET increases (Sykora et al., 2008; Klimpki et al., 2016; Muñoz et al., 2022). Thus, small variations in the measured fluorescence intensity can lead to largely inaccurate results. Moreover, the coloration variability between single $\text{Al}_2\text{O}_3:\text{C,Mg}$ crystals can hinder accurate LET assessment and detector-specific sensitivity correction factors are necessary (Muñoz et al., 2022; Kusumoto et al., 2023). Methods to correct for variable coloration to improve LET determinations have been independently developed (Muñoz et al., 2022; Kusumoto et al., 2023). For LiF and Ag^+ -glass, linear relations between track amplitude and LET have been observed from approximately $10 \text{ keV } \mu\text{m}^{-1}$ up to $200 \text{ keV } \mu\text{m}^{-1}$ in water as illustrated in Fig. 11a (Bilski et al., 2019; Kodaira et al., 2020).

2.6.2. FNTD preparation

Single crystals are typically cut to a size of few millimeters for easier handling; however, the readout process occurs in an area of hundreds of square-microns. Depending on the application, prior to their exposure

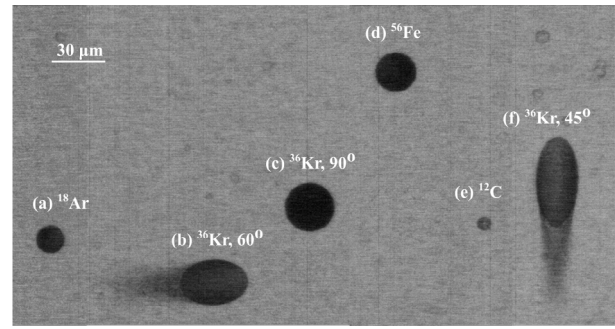


Fig. 12. Examples of tracks in a Harzlas TD-1 track etched detector observed through a microscope for different ions and irradiation angles. (a) shows an ^{18}Ar ion perpendicular to the detector surface at $96 \text{ keV } \mu\text{m}^{-1}$, whereas the effect of irradiations at angles is evident from the ^{36}Kr ions at $443 \text{ keV } \mu\text{m}^{-1}$, where the angles with respect to the surface were (b) 60° (c) 90° (i.e. perpendicular to the surface), and (f) at 45° . (d) shows a ^{56}Fe ion at $198 \text{ keV } \mu\text{m}^{-1}$ and (e) a ^{12}C ion at $13 \text{ keV } \mu\text{m}^{-1}$.

to ionizing radiation, FNTDs can be treated either with heat or UV-light to enhance their sensitivity or improve image-quality metrics.

2.6.3. FNTD properties

The most common devices used to acquire fluorescence intensity images are wide-field and confocal laser scanning microscopes. Except for LiF , where water has a deteriorating effect on the crystal surface, FNTDs can be irradiated submerged in water. After their exposure to ions, the transformed color centers are thermally-stable at room temperatures and can be handled under regular light conditions.

Since LET spectroscopy with FNTDs is performed on a single-track basis, track overlapping can hamper the application of this technique under high particle-fluence conditions. For instance, track overlapping occurs for doses as low as a few milligray for clinical proton beams and for doses up to several centigray for carbon ions, mainly due to the elevated LET of the latter.

For commercial $\text{Al}_2\text{O}_3:\text{C,Mg}$ -based FNTDs, the lower LET detection limit lies approximately at $0.4 \text{ keV } \mu\text{m}^{-1}$ in water (Klimpki et al., 2016). For LiF -based FNTDs, the most recent studies situate the lower limit close to $1.2 \text{ keV } \mu\text{m}^{-1}$ in water (Bilski et al., 2024). In the case of Ag^+ -glass, the lower LET detection limit has been established close to $5 \text{ keV } \mu\text{m}^{-1}$ in water (Kodaira et al., 2020). For Ag^+ -glass, $\text{Al}_2\text{O}_3:\text{C,Mg}$, and LiF no apparent saturation has been observed to LET values as high as (196, 8767, 660) $\text{keV } \mu\text{m}^{-1}$ in water, respectively (Sykora et al., 2008; Bilski et al., 2019; Kodaira et al., 2020).

2.7. Track etched detectors

When high-energy heavy particles pass through a polymer-based track etch detector, they induce microscopic damage to the polymer chains, resulting in the formation of latent tracks (Durrani and Bull, 1987). Chemical etching can be employed to enlarge these latent tracks, since the chemical reactions are more intensive in the damaged regions, revealing dark elliptical objects on the surface. Examples of such tracks viewed under an optical microscope are shown in Fig. 12, for several particles and LET values.

2.7.1. LET determination with track etched detectors

As the rate of etching along the particle track (the track etch rate V_t) is higher than the rate of removing undamaged detector material (the bulk etch rate V_b), the etching process creates a conical-shaped track. To correlate the track morphology to the LET, the parameter V is introduced as

$$V = \frac{V_t}{V_b}, \quad (6)$$

which can be determined through the major and minor ellipsoid axes and the bulk etch (Fleisher et al., 1975). Although V may vary along the ion track, it is commonly considered constant and equal to its average value (Bolzonella et al., 2022; Fleisher et al., 1975). The duration of etching is chosen with regard to achieving optimal parameters for analyzing individual tracks in the given application.

The signals extracted from track etched detectors irradiated with mono-energetic beams with known LET values yield the calibration curves shown in Fig. 13a, where the parameter V is related to the LET across four track etched materials. The materials were produced by different manufacturers as detailed in Brabcová (2010), and their material compositions differ, e.g. through the use of different additives such as antioxidants and plasticizers, curing cycles, or the monomer supply, which all may lead to morphology variations. However, the manufacturers generally do not disclose the exact composition and manufacturing procedures. The relationship between V and the LET can usually be expressed analytically with a polynomial function (Brabcová et al., 2013). Similar LET calibration curves have been established for other materials (Kodaira et al., 2015).

The relationship between the track morphology parameter V and the LET can be used to determine LET spectra. One such example is shown in Fig. 13b, where the LET spectra were measured with TEDs at two positions in a ^{12}C ion beam. For comparison, the figure also shows the LET spectra measured with a Liulin detector at the same positions. For the given combination of material, detector etching and analysis, the lower LET limit of the TEDs was $7\text{ keV }\mu\text{m}^{-1}$ (Brabcová et al., 2013). However, a lower LET limit of $5\text{ keV }\mu\text{m}^{-1}$ with TEDs is achievable (Hirano et al., 2018).

2.7.2. Track etched detector properties

The track etched detectors can detect particles with LET above the detection threshold, which depends on the used material and evaluation conditions. For the most sensitive PADC (poly allyl diglycol carbonate) materials, it is around $(5\text{--}10)\text{ keV }\mu\text{m}^{-1}$. Particles with lower LET and indirectly ionizing particles such as neutrons or photons can be registered via secondary heavy-charged particles created in nuclear interactions with the detector's material or surroundings. It should be noted that there exists an angle threshold for track formation, the so-called critical angle, between the trajectory of the particle producing a track and the surface of the detector, below which the tracks cannot be detected. More information about the PADC-based track detectors can be found in, e.g., Bolzonella et al. (2022).

The optimal fluence range of directly registered heavy charge particles is in the order of 10^3 to 10^5 particles/cm². Similarly to the luminescence detectors in Section 2.1 and the FNTDs in Section 2.6, the track overlap depends on both the particle fluence and the particle track structures. As the tracks start to overlap, it gradually becomes difficult or impossible to distinguish them from one another. For example, for carbon ions with LET values near $30\text{ keV }\mu\text{m}^{-1}$ in water, the track overlapping represents a severe problem for fluences above 10^6 particles/cm² which corresponds to around 50 mGy (Osinga et al., 2014). However, as the track size depends on the etching procedure, a combination of short etching times and atomic force microscope (AFM) analysis can enable measurements of a fluence up to 10^8 particles/cm² (Johnson et al., 2009). Kodaira et al. (2013) showed track morphology was in good agreement for detectors etched shortly and analyzed with AFM and detectors etched longer and analyzed with an optical microscope system.

To avoid exposure to radon and reduce the effects of aging, fading, and environmental influences, the track etched detectors should be stored in radon-proof bags at freezing temperatures before use. The detectors can be cut to the required dimensions by hand. Typically, the area of the analyzed detector surface needs to be of the order of 10^{-1} cm^2 to ensure reasonable counting statistics. The track etched detectors have been used extensively for assessment of LET spectra in light ion beams (Brabcová et al., 2010; Kodaira et al., 2015; Oancea et al., 2018; Hirano et al., 2018; Kodaira et al., 2019).

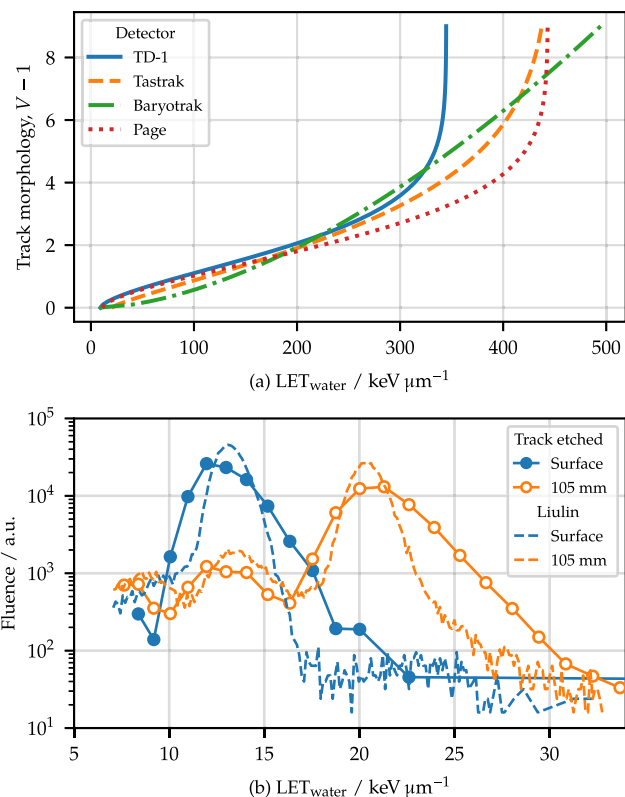


Fig. 13. (a) Relationship between the track morphology V defined by Eq. (6) and the LET in four track etched detector materials. (b) Examples of LET spectra derived with a track etched detector in a ^{12}C 290 MeV/u beam. The measurements were undertaken at two depths; one at the surface and another at 105 mm water-equivalent depth. The track etched detector measurements are shown with markers, and lines to assist the eye, and compared to the spectra measured with an Si-diode based detector (Liulin, dashed lines).

Source: Data from Brabcová (2010) and Brabcová et al. (2010).

2.8. Alanine detectors

Alanine is a passive chemical detector in which stable radicals are formed upon irradiation with ionizing radiation. Subsequent electron paramagnetic resonance (EPR) is applied to determine the radical yield, which generally is proportional to the absorbed dose. It is well established that alanine quenches for increasing LET, but LET may also be determined without prior knowledge of dose (Hansen and Olsen, 1985; Malinen, 2014).

2.8.1. LET determination with alanine

EPR dosimetry has shown distinctive signal characteristics for ion-irradiated materials that differ from those after photon irradiation. This has been attributed to the spatial distribution of radicals along ion tracks, providing a distinct signature that could help identify the radiation type responsible for radical formation (Ciesielski and Wielopolski, 1994; Ciesielski et al., 1998). Microwave power saturation analysis, a technique where samples are subjected to varying microwave power levels, can yield information on the spin populations within an EPR signal. This is achieved by modeling and fitting to the experimental data to estimate relaxation times T_1 and T_2 , indicative of the interaction between spin states and the lattice or other spins, respectively (Malinen, 2014).

Research by Krushev et al. (1994) and subsequent studies have found that the microwave power saturation behavior differs between ions and γ -rays, reflecting variations in radical concentration and relaxation dynamics due to ion track structures. Notably, high-LET radiation

results in more slowly saturating EPR signals compared to low-LET γ -rays, as seen with helium versus proton irradiation. Further exploration of these phenomena indicates that parameters such as the ratio of intensities of the main and satellite EPR lines (the so-called x/y ratio) could serve as indicators of the LET, with lower ratios corresponding to higher-LET radiation. Nakagawa et al. (2008) explicitly related EPR spectra to the LET of heavy ions for alanine.

2.8.2. Alanine detector properties

The microwave power saturation and the x/y ratio of the EPR signal has, however, received limited attention, but is summarized in Malinen (2014). The same reference concludes that even if alanine is more suited for high-dose irradiation, it may offer estimations of the radiation quality at clinical dose levels. This was demonstrated in studies with 20 Gy doses, suggesting the viability of these methods in a clinical setting.

Other radical forming chemicals which were investigated include lithium formate monohydrate (Waldeland et al., 2010), ammonium tartrate (Marrale et al., 2006, 2014), sucrose (Nakagawa et al., 2008), and potassium dithionate (Gustafsson et al., 2011), where the latter explicitly highlights the possibility of determining dose and LET simultaneously.

3. Active detectors for LET assessment

Active detectors for measurements of microdosimetric spectra rely on the energy depositions in sensitive volumes (SV). The SVs are generally manufactured to an extent or a density that simulates biological target sizes at a micrometer level, i.e. at the level of a cell nucleus. With the improvements in nanotechnologies, silicon-based microdosimeters utilize SVs of few micrometers in diameter, enabling pixelated measurements. On the other hand, for gas-filled microdosimeters operated as a proportional counter, the cavity can be manufactured with a 1 mm diameter, which enables a simulation of biological target sizes of 1 μm diameter or less through a reduced gas pressure. This section outlines radiation quality determinations using miniaturized tissue-equivalent proportional counters (TEPCs) and two silicon microdosimeters, as shown in Fig. 14. An active analog of the passive track detectors described in Sections 2.6 and 2.7, the Timepix detector, is included for comparison.

3.1. The mini-TEPC

The first miniaturized TEPC was developed at Columbia University in the 1980's by Kliauga (1994). It was later simplified by De Nardo et al. (2004), before being redesigned as a sealed TEPC to operate without gas flow (Conte et al., 2019). The mini-TEPC is shown in Fig. 14a, and further details can be found in Conte et al. (2019).

As for the other microdosimetric detectors herein, the results are given in terms of frequency, $f(y)$, or dose distributions, $d(y)$, of the lineal energy y , which, in a first approximation, is the stochastic equivalent of LET.

3.1.1. Mini-TEPC microdosimetric spectra

The mini-TEPC has been used to assess the microdosimetric quantities in proton beams as shown in Fig. 15. In this figure, the measurements were conducted with the detector positioned behind solid water plates, but the detector can also operate when placed inside a water phantom. The microdosimetric spectra acquired at six positions along central beam axis of a spread out Bragg peak (SOBP) are shown in Fig. 15a. In proton and light ion beams, the mean values of the measured distributions in frequency and dose provide estimates of the $\overline{\text{LET}}_F$ and $\overline{\text{LET}}_D$, respectively.

An example is shown in Fig. 15b, where the radiation quality was measured at over 100 points in water. Due to its high sensitivity, the detector is capable of measuring single ionization events, which correspond to detectable lineal energy values down to 0.05 $\text{keV } \mu\text{m}^{-1}$ in water.

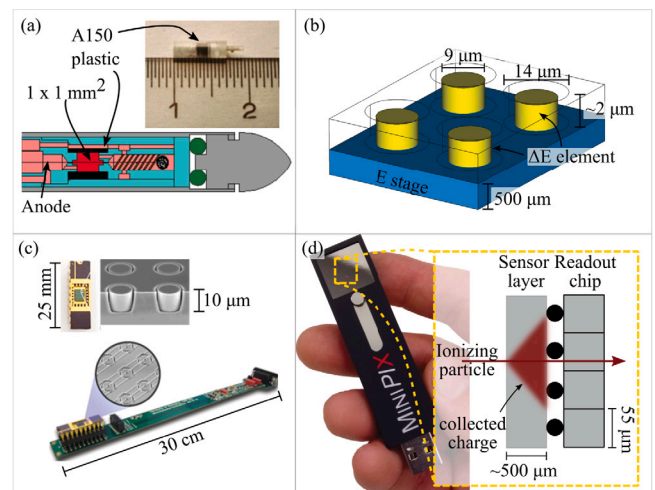


Fig. 14. Overview of the three microdosimetric detectors and the active Timepix detector. (a) Photo of the mini-TEPC internal sensor housed in a thin aluminum shell with an outer diameter of 15 mm detailed in Section 3.1. A detailed explanation of the figure can be found in Conte et al. (2019). (b) Technical sketch of the silicon telescope in Section 3.2, which consists of so-called ΔE -elements. (c) Photos and sketches of the SOI mushroom microdosimeter and the MicroPlus probe described in Section 3.3. (d) Photo of a Timepix chip, connected to a MiniPix readout interface, with a schematic view of the sensitive silicon-layer, where the particle charge is spread over several pixels. The Timepix detector is detailed in Section 3.4.

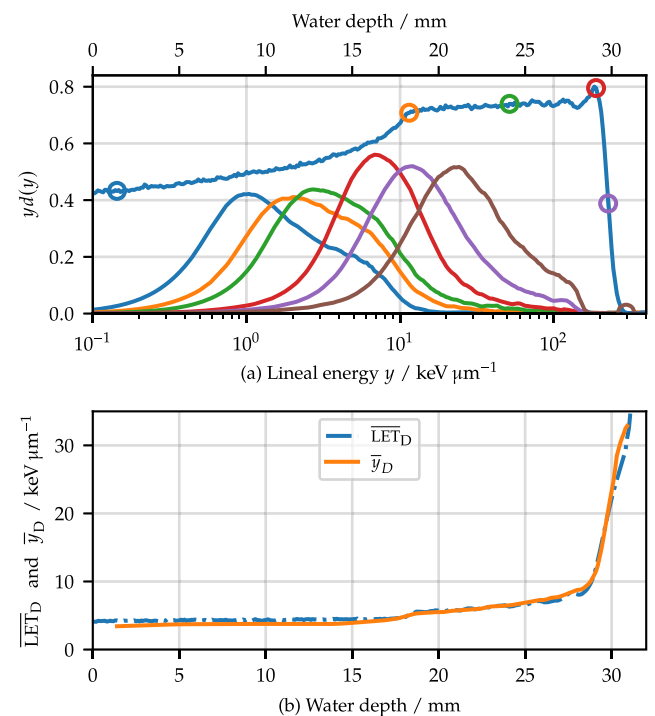


Fig. 15. (a) Microdosimetric spectra measured at six positions (indicated by open circles) in a 60 MeV proton spread-out Bragg peak (SOBP). The relative depth dose distribution is plotted for reference, where the marker color of the circles refer to the positions of the spectra. (b) Measured mean-dose lineal energy (\bar{y}_D) and simulated dose-averaged LET ($\overline{\text{LET}}_D$) along the central beam axis of the SOBP outlined in (a). Source: Data from Conte et al. (2019) and Bianchi et al. (2021).

3.1.2. Mini-TEPC properties

The lineal energy in light ion beam can be measured by filling a Mini-TEPC with propane gas at 408 mbar, and applying a high voltage (600–800 V) to the cathode. With these conditions, a measurement takes around 1 min (Conte et al., 2020). The onset of a gas avalanche

process ensures that the initial number of electrons produced in the gas cavity during each energy deposition event is multiplied by an average gain factor, whose role is to enhance the detector sensitivity. This factor typically falls within the range of 100 to 2000, depending on the applied voltage. The detector operates in proportional mode, which means that the collected number of electrons is proportional to the initial number. The description of the proportional counter is detailed in Knoll (2010), and the detector is able to simulate $1\ \mu\text{m}$ of biological tissue. The primary limitation of gas detectors is their fluence rate capability, which is typically restricted by a maximum count rate of 30 kcounts/s. For example, the measurements shown in Fig. 15a were acquired at a constant dose-rate, corresponding to approximately 30 mGy/s at the Bragg peak.

3.2. The silicon telescope

The current version of the silicon telescope detector is the result of decades of development. The first version of the monolithic detector — obtained by implanting a p^+ electrode on a single silicon crystal — was designed by Cardella et al. (1996) and manufactured by ST Microelectronics (Catania, Italy). Notably, it was originally intended for charged particle discrimination. Later, Agosteo et al. (2006) proposed to employ the so-called ΔE element as a microdosimeter. The ΔE and the E elements are separated by a deep-implanted p^+ electrode which acts as a watershed for charge collection. Measurements with this silicon telescope in a clinical parallel proton beam have been demonstrated to agree with a mini-TEPC detector described in Section 3.1 (Agosteo et al., 2010).

However, this version of the silicon telescope showed some limitations in isotropic irradiation fields as the length of a tilted particle track in the SV can exceed millimeters (Agosteo et al., 2006). The latest iteration of the silicon detector was proposed by Agosteo et al. (2008), where the pixelated silicon microdosimeter minimizes those effects (see Fig. 14b for a graphical representation). To achieve SV's sizes needed to simulate biological sites according to the simulation principle in Section 1.1, the ΔE element dimensions were reduced. This latest development consists on a matrix of cylindrical ΔE elements and a single residual-energy E stage (about $2\ \mu\text{m}$ and $500\ \mu\text{m}$ in thickness, respectively). The E stage plays a fundamental role in assessing the full energy of the interacting particles, as it allows for an LET-dependent correction for tissue-equivalence to be performed event-by-event.

3.2.1. Telescope microdosimetric spectra

The minimum detectable lineal energy with the silicon telescope detector is about $8\ \text{keV}\ \mu\text{m}^{-1}$ in silicon, limited by the electronic noise. Therefore, the silicon detector is limited to measurements of protons at the distal part of the Bragg peak or heavier particles as carbon ions. An example of a measured microdosimetric spectrum in a clinical proton beam is shown in Fig. 16a. The silicon telescope determined spectrum is in agreement with a reference TEPC (Agosteo et al., 2010). The same work also demonstrated a good agreement between average microdosimetric quantities, such as the \bar{y}_D derived from the spectrum.

Furthermore, the $\Delta E - E$ telescope structure allows to discriminate between charged particles. Therefore, different types of nuclear fragments, arising from the fragmentation of the primary ions and of the target nuclei, can be detected, see Agosteo et al. (2011) for details. Fig. 16b highlights an example of \bar{y}_D measurement with the silicon telescope compared to the simulated $\overline{\text{LET}}_D$ in a 62 MeV/u ^{12}C beam. Measurements with the mini-TEPC are included for comparison.

Further microdosimetric measurements have also been performed in hadron beams by placing the detector behind a phantom made of PMMA layers, see details in Agosteo et al. (2010, 2011), Bianchi et al. (2020, 2021), Colautti et al. (2020, 2018a,b).

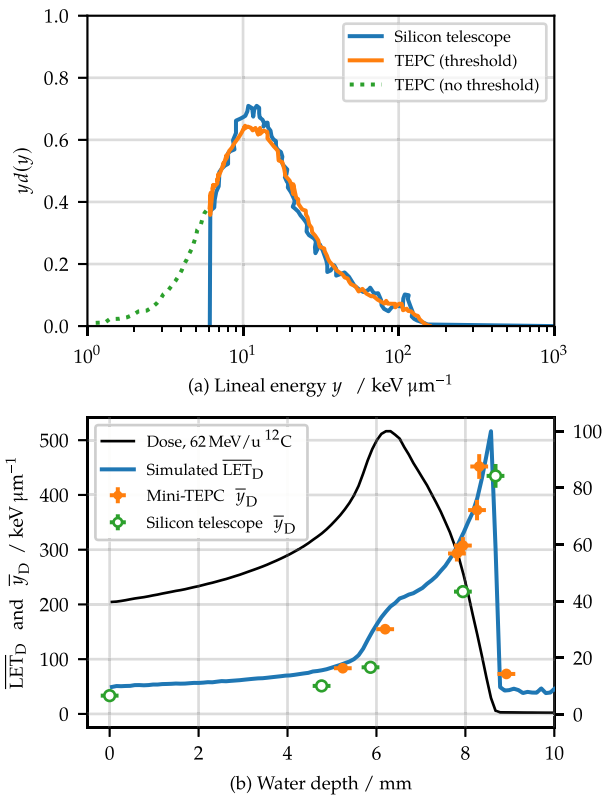


Fig. 16. (a) Example of a microdosimetric spectrum measured in the distal part of a therapeutic proton beam compared with the one acquired with the mini-TEPC in Section 3.1. (b) Shows the possible \bar{y}_D measurements with the silicon telescope and the mini-TEPC along the central beam axis of a 62 MeV/u carbon ion beam, where the simulated dose and $\overline{\text{LET}}_D$ distributions are included for reference. Source: Data from Agosteo et al. (2010) and Colautti et al. (2018b).

3.2.2. Silicon telescope properties

The detector enables high-resolution LET determinations in the range $8\ \text{keV}\ \mu\text{m}^{-1}$ to $1000\ \text{keV}\ \mu\text{m}^{-1}$ in silicon. The pixelated detector consists of a matrix of cylindrical ΔE elements (about $2\ \mu\text{m}$ in thickness) and a single residual-energy E stage ($500\ \mu\text{m}$ thick). The nominal diameter of the ΔE elements is about $9\ \mu\text{m}$ and the width of the pitch separating the elements is about $41\ \mu\text{m}$. More than 7000 pixels are connected in parallel to give an effective sensitive area of about $0.5\ \text{mm}^2$. A guard ring hinders charge collection outside the SV. The geometry therefore reduces de facto the mean chord length of each ΔE element to about $2.8\ \mu\text{m}$, thus mitigating adverse effects in non-isotropic fields.

3.3. SOI mushroom microdosimeter

The silicon microdosimetry concept was introduced by the Center for Medical Radiation Physics (CMRP, University of Wollongong) in 1996 where $p-n$ junctions of source and drain of the MOSFET were used as micrometer-sized SVs to provide microdosimetric measurements in a neutron beam for fast neutron therapy.

This approach was improved by the development of an array of micrometer-sized silicon SVs to mimic an array of biological cells. The SVs were fabricated on a silicon on insulator (SOI) substrate. Five generations of SOI microdosimeters have been developed, fabricated and successfully tested in particle therapy and space radiation environments (Rosenfeld, 2016). The latest generation of the SOI microdosimeter developed by the CMRP is called the *Mushroom microdosimeter* and is shown in Fig. 14c. The complete system with readout electronics is referred to as the *MicroPlus probe*. The SOI Mushroom microdosimeters

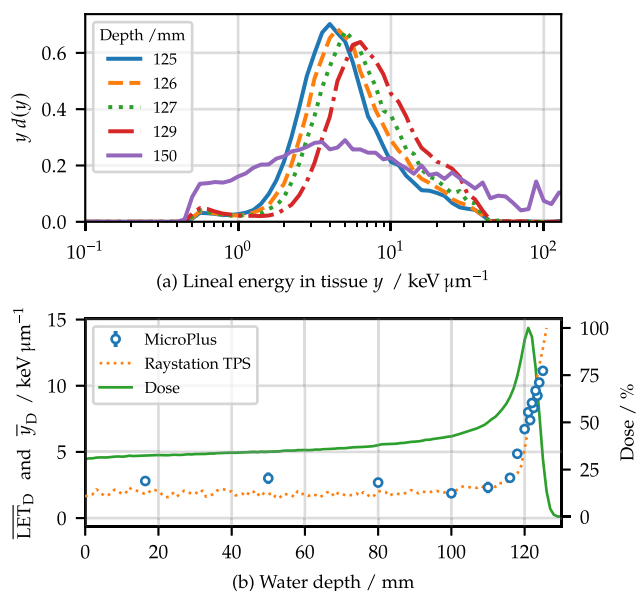


Fig. 17. (a) Microdosimetric spectra measured with the MicroPlus detector at different depths in a water phantom along 131 MeV proton spot scanning beam. (b) Determination of \bar{y}_D to water with the MicroPlus detector along the central axis of a proton beam. The simulated \overline{LET}_D and dose with the Raystation treatment planning system is shown for comparison.

Source: Data from Tran et al. (2017) and Wagenaar et al. (2020).

are fabricated using a so-called 3D Micro Electro Mechanical Systems (MEMS) 3D detector technology at the SINTEF MiNaLab, Norway. This technology allows well-defined 3D SV microdosimeter to be produced to overcome the charge sharing issues between SVs encountered in previous generations of microdosimeters. The cylindrical SVs were fabricated in different sizes and configurations with diameters between 18 μm to 30 μm , thicknesses of 2 μm to 50 μm and at a pitch of 50 μm in matrices of 20 \times 20 or 50 \times 50 SVs (Tran et al., 2021). The SVs were segmented into sub-arrays to reduce capacitance and avoid pile up in high dose-rates. Furthermore, the different SV diameters enables a study of the effect of the chord length. The configurations have been employed for various applications, for example field dosimetry in particle therapy or space applications with much lower dose-rates (Rosenfeld, 2016).

3.3.1. MicroPlus probe microdosimetric spectra

The MicroPlus probe is operated with a low-voltage battery which enables it to be used in clinical settings with a high degree of portability. Enclosed in a water-proof PMMA sheath, it can be operated in water phantoms. Examples of measurements of microdosimetric spectra obtained with the MicroPlus probe are shown in Fig. 17a. These measurements were undertaken along the central axis of a proton beam at 131 MeV proton beam. An example of measurements of \bar{y}_D to water compared to simulated \overline{LET}_D is shown in Fig. 17b.

3.3.2. MicroPlus probe properties

With its small millimeter-sized chip and only a small number of connected SVs, the MicroPlus probe provides an ability to measure microdosimetric spectra with a high spatial resolution at high dose-rates (10^8 particles/s). The use of a low-noise pre-amplifier and shaping amplifier enables detection of lineal energies in tissue as low as 0.3 $\text{keV } \mu\text{m}^{-1}$, and down to $\sim 0.15 \text{ keV } \mu\text{m}^{-1}$ in water cooled to approximately 10 $^\circ\text{C}$. The detector type was used to measure the LET relevant to Xe-124 ions (James et al., 2019) but does not in principle have an upper limit for LET determinations. However, the LET determination requires a conversion from silicon to tissue or water.

3.4. The Timepix detector

The Medipix Collaboration at CERN has developed a series of Timepix detector technologies, starting from Timepix (Llopert et al., 2007) and up to the current generation of Timepix4 (Llopert et al., 2022). The aim was to make radiation detection technologies, originally developed for high-energy physics research, accessible to a wide range of applications. The operating principle of the hybrid detector Timepix relies on the coupling of a sensitive volume (e.g. semiconductor) with a chip for pixelated measurements of single particle tracks. The chips enable single photon counting, measurements of the time-of-arrival and of the generated electron-hole pairs for single particles in the sensitive volume. The latter allows for a calibration between the collected charge and the energy deposition in the sensitive volume at a per-pixel level (Jakubek, 2011). The determination of the energy deposition from a single particle track can be related to the LET either in semiconducting sensors (Ploc et al., 2018) or in gaseous media (Leidner et al., 2021). A photo of a Timepix chip equipped with a silicon sensor is shown in Fig. 14d and is by far the most investigated configuration — with respect to sensitive material and Timepix generation — for ion radiation measurements (Granja et al., 2011; Stoffle et al., 2015; Gehrke et al., 2017; Nabha et al., 2022; Stasica et al., 2023). However, first studies using third-generation Timepix chips for LET assessment have recently been reported (Oancea et al., 2023; Félix-Bautista et al., 2024). The Timepix detector, operated in the so-called time-over-threshold (ToT) mode, is capable of determining a particle's energy deposition in the sensitive volume. The reader is referred to Jakubek (2011) for a discussion on ToT and its relation to the energy deposition.

3.4.1. Timepix measurements

Irradiation of a Timepix detector with protons and heavier ions results in the dispersion of charge across multiple adjacent pixels. This phenomenon primarily arises from charge repulsion and diffusion within the sensor (Granja et al., 2011; Šolc et al., 2022), and these groups of neighboring pixels with energy depositions above the detection threshold of typically 5 keV are referred to as clusters that can be related to the LET. Examples of clusters for irradiations with low-LET protons and high-LET carbon ions are shown in Fig. 18.

One challenge with semiconductor detectors is that of saturation effects at high local energy depositions relevant to the track center of high-LET particles. For Timepix detectors, a relevant saturation effect occurs for energy depositions $\geq 1 \text{ MeV}$ per pixel. The saturation mostly affecting the central pixels of the cluster is referred to as the volcano effect after its shape. It poses a challenge for dosimetry in hadron beams relevant to particle therapy and space applications (Gehrke et al., 2017; George et al., 2018; Sommer et al., 2022).

The saturation effect is attributed to the chip circuit rather than saturation effects in the sensor itself (Abu Al Azm et al., 2016). Currently, this challenge is handled in different ways. Firstly, circuit improvements in the Timepix generations 2 and 4 are expected to improve the response to high-LET particles by implementing an adaptive gain in the analog circuit of each pixel (Llopert et al., 2022; Wong et al., 2020). Likewise, the sensor thickness can be reduced to 0.1 mm to reduce the deposited energy, the detector can be irradiated at larger polar angles, or the pixels can be calibrated at energies $\geq 1 \text{ MeV}$, beside a partial sensor depletion (Granja et al., 2021; Sommer et al., 2022). An optimal combination of the available setting parameters depends on the LET range under investigation.

Studies have demonstrated how Timepix detectors can be used for dosimetry in protons, helium, and carbon ions (Gehrke et al., 2017; Granja et al., 2018; Nabha et al., 2022). One such example is shown in Fig. 19 for particles spanning the LET range of 0.7 $\text{keV } \mu\text{m}^{-1}$ to 57 $\text{keV } \mu\text{m}^{-1}$ in silicon, where the measurements were acquired with a partially depleted chip to minimize the volcano effect. This LET range corresponds approximately to 0.4 $\text{keV } \mu\text{m}^{-1}$ to 30 $\text{keV } \mu\text{m}^{-1}$ in water. The measured cluster energy in Fig. 19 is correlated to the Monte

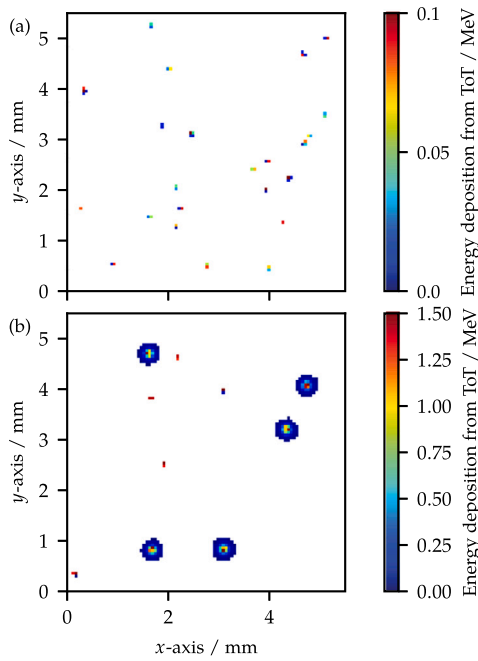


Fig. 18. Examples of Timepix measurements with (100×100) pixels corresponding to (5.5×5.5) mm² in (a) low-LET protons at 221 MeV/u and (b) high-LET carbon ions at 89 MeV/u. The energy deposition of each ion is best represented as the sum of the energy depositions of all pixels in each cluster.

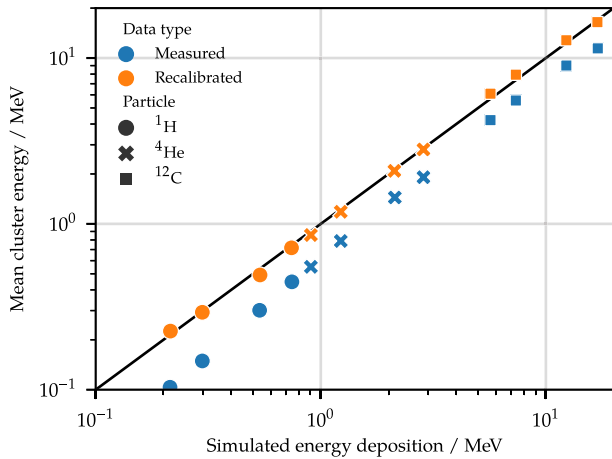


Fig. 19. Correlation between measured energy deposition in clusters and Monte Carlo simulated energy deposition for protons, helium, and carbon ions. The measured data was acquired with a partial depletion of the sensor layer, which required a linear recalibration to establish the agreement indicated by the solid line within 7% with respect to the simulated energy deposition. The recalibrated energy deposition can be used to determine LET.

Source: Figure adapted from Gehrke et al. (2017).

Carlo simulated energy deposition as detailed in Gehrke et al. (2017). The results show an agreement between the measured and simulated energy depositions within 7% across the investigated ion types and initial energies, which can be used to determine the LET with similar accuracy (Stasica et al., 2023; Nabha et al., 2022).

Fig. 20 showcases the measurement of LET spectra in two different proton fields (Nabha et al., 2022). The low-LET spectrum ($\overline{\text{LET}}_F \approx 0.8 \text{ keV } \mu\text{m}^{-1}$) is acquired through an irradiation with 200 MeV protons with the detector surface placed at an angle $\varphi = 73^\circ$. A second LET spectrum with $\overline{\text{LET}}_F \approx 3.2 \text{ keV } \mu\text{m}^{-1}$ was acquired in a 31 MeV

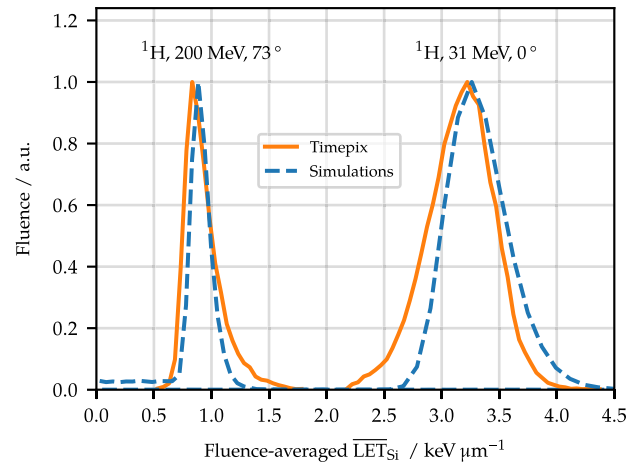


Fig. 20. Two examples of LET spectra assessed with a Timepix detector (solid line) and acquired through simulations (dashed lines). The left spectrum was acquired for 200 MeV protons at an inclination of $\varphi = 73^\circ$ and the right for 31 MeV protons perpendicular to the sensor surface ($\varphi = 0^\circ$). Source: Data from Nabha et al. (2022).

beam orthogonal to the sensor surface, i.e. $\varphi = 0^\circ$. Both LET spectra were validated with Monte Carlo particle transport simulation methods, illustrated in the figure with dashed lines (Nabha et al., 2022).

To specify the measurable LET range in a more general form, the lower LET limit can be estimated by the minimal energy deposition of $\sim 5 \text{ keV}$ over the usual sensor thickness of $300 \mu\text{m}$, i.e. $\sim 0.01 \text{ keV } \mu\text{m}^{-1}$ in water. The upper LET limit, based on the highest recently reported LETs in George et al. (2018) and Granja et al. (2018) ranges from $50 \text{ keV } \mu\text{m}^{-1}$ for angles of incidence that are perpendicular to the sensor surface (i.e. for small polar angles $\varphi \approx 0^\circ$) up to $250 \text{ keV } \mu\text{m}^{-1}$ in water for optimized conditions of large polar angles $\varphi > 60^\circ$ and saturation compensation strategies as described in George et al. (2018).

3.4.2. Properties of the first-generation timepix detector

The Timepix detector consists of a sensitive layer and a chip area of 2 cm^2 with > 65000 pixels that are $(55 \times 55) \mu\text{m}^2$ in size. The thickness of the silicon sensor can vary between $(0.1\text{--}1) \text{ mm}$ with a detection efficiency of protons and heavier ions close to 100%. Whilst the detection efficiency is in principle dose independent, it may be affected by the dose rate through track overlaps that affect the cluster size and measured energy deposition. The data acquisition is based on frames with an adjustable frame duration. Commercial readout interfaces enabling acquisitions of up to 1700 frames/s are also available (Turecek et al., 2016). The fluence-rate at which particle tracks start to overlap strongly depends both on the particle field and detector settings and properties. E.g., for a silicon sensor of $300 \mu\text{m}$ thickness operated at 5 keV energy threshold, bias voltage of 10 V and 1 ms frame duration, signal overlaps stay below 3% at fluence rates $\sim 10^4$ particles/s/cm² for ions lighter than carbon ions.

4. Discussion

The macroscopic radiation quality metric LET (or, averaged LET) can be assessed through measurements with the detectors presented herein, and several of them enable simultaneous dose and LET determination with a single detector. The properties of the detectors, however, vary tremendously, which means a detector for LET assessment should be chosen with care depending on the irradiation conditions. The following section compares the detector properties and provides recommendation on their use.

Table 1

Overview of passive detectors to assess $\overline{\text{LET}}$ of ions with a single detector, where the absorbed dose does not need to be known a priori. All detectors are in principle dose-rate independent but their response is affected by track overlap above a certain fluence limit. For luminescent detectors, the track overlap affects the LET determination and depends on the dose above a certain threshold. For FNTDs and track-etched detectors (TEDs), track overlap limits the track identification. The upper LET measurement limit for FNTDs merely represent the highest tested values, where no signal saturation was observed. The use of RPLDs and chemical detectors such as alanine has seen little use for $\overline{\text{LET}}$ assessment.

Detector	Section	Material	Fluence limit ^a (particles/cm ²)	Measurable LET _{water} (keV μm^{-1})	Dimensions (mm ³)	Commercially available	Selected reference
OSLD	2.2	Al ₂ O ₃ :C	$< 5 \times 10^9$	0.2 to 4×10^1	$\varnothing 2 \times 0.1$	Yes	Granville et al. (2016)
OSLD	2.2	Al ₂ O ₃ :C,Mg	$< 5 \times 10^9$	0.2 to 5×10^1	$\varnothing 2 \times 0.1$	Yes	Christensen et al. (2023)
TLD	2.3	LiF:Mg,Ti	$< 5 \times 10^9$	0.2 to 1×10^2	$\varnothing 3.2 \times 0.3$	Yes	Bilski (2010)
RPLD ^b	2.4	Ag ⁺ -glass	–	–	$\varnothing 1.5 \times 8.5$	Yes	Miyamoto et al. (2014)
FNTD	2.6	Al ₂ O ₃ :C,Mg	$< 10^7$	0.4 to $> 8 \times 10^3$	$4 \times 8 \times 0.5$	Yes	Muñoz et al. (2022)
FNTD	2.6	LiF	$< 10^7$	1 to $> 5 \times 10^2$	$3 \times 3 \times 0.5$	Yes	Bilski et al. (2019)
FNTD	2.6	Ag ⁺ -glass	$< 10^7$	10 to $> 1 \times 10^2$	$8.5 \times 8.5 \times 1.5$	Yes	Kodaira et al. (2020)
TED ^c	2.7	Plastic	$< 10^7$	5 to $> 3 \times 10^2$	$10 \times 10 \times 0.9$	Yes	Brabcová et al. (2010)
EPR ^d	2.8	Alanine	$> 10^{11}$	> 10	$\varnothing 5 \times 2$	Yes	Malinen (2014)

^a OSLDs, TLDs, and RPLDs are applicable for LET determinations below ≈ 2 Gy in fast protons and ≈ 10 Gy in ¹²C ions.

^b Not yet suitable for assessment of $\overline{\text{LET}}$, although features in the RPL spectrum can be related to the radiation quality.

^c Track-etched detectors can be applied in fluences up to 10^8 particles/cm² with an optimized process.

^d Alanine detectors are capable of LET determinations at ≈ 20 Gy through EPR signal parameters but further studies are needed.

4.1. Passive detectors

An overview of the passive detectors available for $\overline{\text{LET}}$ determination, for which $\overline{\text{LET}}$ can be evaluated with a single detector, is provided in Table 1. The indirect determination of $\overline{\text{LET}}$, where the reduced detector efficiency is used to estimate the $\overline{\text{LET}}$ through an a priori knowledge of the dose, is not covered herein.

The luminescence detectors in Table 1 enable point-like determinations of the radiation quality, e.g. through LET_F or LET_D . One of the key advantage of luminescence detectors is their passive nature, which enables the detectors to be embedded inside objects, e.g. in anthropomorphic phantoms, with a minimal disturbance of the radiation field. Together with their dose-rate independence, this makes luminescence detectors suitable for dose and $\overline{\text{LET}}$ determination under clinically relevant conditions, thus addressing the needs for ion beam dosimetry defined in Vedelago et al. (2022). However, one challenge with luminescence detectors is that their response depends on both the dose and $\overline{\text{LET}}$. This means that overlapping particle tracks can perturb the local ionization densities and thus the detector response in a fashion similar to LET variations. This track overlap restricts the ability of luminescence detectors to accurately assess $\overline{\text{LET}}$ above a certain fluence threshold. For OSLDs, RPLDs, and TLDs, this threshold is of 1 Gy to 2 Gy in fast protons and > 10 Gy in fast ¹²C ions, above which $\overline{\text{LET}}$ determinations require dose corrections.

While chemical detectors as alanine have been demonstrated to be capable of $\overline{\text{LET}}$ assessment with a single detector through analysis of the EPR signal (Malinen, 2014), further studies are needed to fully assess their capability to determine LET at clinically relevant doses.

FNTD and TED detectors both enable determination of the LET spectrum, but the use of these detectors for measurements in beams of clinically relevance is limited due to track-overlaps. The determination of a LET spectrum allows to overcome some of the challenges related to generating predictive models e.g. for RBE, since no single-valued (and measurable) parameter has yet been identified, which reliably can be used as a radiation quality metric input parameter, as discussed further in Kalholm et al. (2022).

While the luminescence detectors provide excellent properties for experiments without time constraints, the somewhat slow read-out procedures and post-processing makes them difficult to use for e.g. daily quality assurance (QA) in a clinical setting. On the other hand, they are applicable for accurate and point-determinations of averaged LET, suitable for postal LET audits, commissioning of TPS LET-calculations, yearly QA, and research projects.

4.2. Active detectors

The three microdosimetric detectors in Section 3, one mini-TEPC and two based on silicon-cylinders, enable measurements of the lineal energy spectrum in micrometer-sized sensitive volumes (SVs). Therefore, these detectors provide more information than just an averaged quantity, similar to the TED and FNTD among the passive detectors in Section 4.1. Still, the mean lineal energy \bar{y} may be derived from these spectra, which can be related to the $\overline{\text{LET}}$ and cell survival curves (Kase et al., 2006). Another type of active detector, the Timepix, provides not only an estimate of LET spectra but also particle discrimination. Table 2 provides an overview of the active detector properties.

Although the mini-TEPC is sensitive to pile-up effects in clinically relevant fluence-rates, its tissue-equivalence and the small extend of the SV enable \bar{y} measurements of interest to clinical proton fields. The silicon-based microdosimeters in Sections 3.2 and 3.3, particularly the SOI Mushroom, enable measurements at clinically relevant conditions, but requires a conversion from the energy deposition in silicon to that in water or tissue. Another, recently developed microdetector, based on multi-arrays (Bachiller-Perea et al., 2022), exhibited promising results for spatially-resolved measurements. Other microdosimetric detectors are detailed in Parisi et al. (2022c).

The prompt data acquisition, however, makes the active detectors appealing for patient specific QA in clinical settings. Nonetheless, as of today, only the Timepix detector is commercially available (see Table 2).

4.3. Assessing LET-to-medium

The possibilities to determine LET to a given medium, typically to water or tissue, may be affected by the use of detectors composed of materials different from the one of interest. Particularly nuclear reactions in the detector material may result in target fragmentation, where high-LET fragments could affect the assessment of LET to the medium of interest (Kalholm et al., 2021). For a simple comparison between detectors and systems, it is possible to report the LET-to-water, even for non-water media.¹ Hence, LET detector types, which do not require large energy dependent corrections, have an advantage. This is analog to dosimetry, where air-filled ionization chambers are preferred due to their water equivalence for a wide range of energies and charged particles.

¹ This is the default for TPSs capable of calculating LET distributions in patients, such as the research version of Raystation.

Table 2

Comparison of the active detectors, three relying on microdosimetric spectra and one on single track analysis. For sensitive volumes (SVs) different from the medium of interest, typically tissue or water, a conversion to that medium is required. The tissue equivalent (TE) size is estimated for each SV. The fluence-rate limit denotes an approximate upper measurement limit for each detector type. $\text{LET}_{\text{water}}$ is an estimate of the measurement range at which LET or \bar{y} can be determined.

Detector	Section	Micro-dosimeter	Material of SV	TE	TE SV size (μm)	Fluence-rate limit ^a (particles/cm ² /s)	Measurable $\text{LET}_{\text{water}}$ (keV μm^{-1})	Commercially available	Selected reference
Mini-TEPC	3.1	Yes	Variable ^b	Yes	0.5–2	$< 5 \times 10^6$	Full spectrum ^c	No	Conte et al. (2020)
Si-Telescope	3.2	Yes	Silicon	No	3.2	$< 10^4$	6 to 3×10^3	No	Agosteo et al. (2006)
SOI MicroPlus	3.3	Yes	Silicon	No	3.4	$< 10^8$	> 1	No	Rosenfeld (2016)
Timepix	3.4	No	Silicon/gas	No	N/A	$< 5 \times 10^4$	0.01 to 5×10^d	Yes	Gehrke et al. (2017)

^a A 1.5×10^9 particles/cm²/s fluence-rate of 230 MeV protons in water corresponds to $\approx 1 \text{ Gy s}^{-1}$

^b The gas composition and pressure can be adjusted to acquire measurements with e.g. tissue- or water-equivalency.

^c The voltage of the mini-TEPC can be adjusted to enable measurements of the full LET range.

^d LET limits are quantified as described in Section 3.4.1.

4.3.1. LET-to-medium with passive detectors

Passive luminescence detectors for $\overline{\text{LET}}$ assessment are often composed of materials heavier than tissue, see e.g. OSLD based on Al_2O_3 in Section 2.2 or TLDs based on LiF in Section 2.3. However, to assess LET with these detectors, luminescence features are calibrated directly against the radiation quantity of interest, e.g. $\overline{\text{LET}}_D$ in water or medium, where the radiation quality typically is obtained through Monte Carlo simulation methods. The luminescence features may be distorted through nuclear reactions with materials different from the one of interest. Nonetheless, fragments heavier than the primary particles contribute little to the dose, and their contribution to the luminescence signal is further suppressed by ionization quenching caused by their high LET (Muñoz et al., 2024b). As a result, the effect of target fragmentation for the assessment of $\overline{\text{LET}}$ to a certain medium is generally negligible for OSLDs, TLDs, and RPLDs.

FNTDs and TEDs assess $\overline{\text{LET}}$ through spectra acquired against reference measurements as exemplified in Section 2.5. Target fragmentation could result in heavy secondaries recorded in the analyzed volume, that would not be present in water or tissue, which eventually could bias the averaging of the LET spectrum. However, both detector types generally record particle tracks within a $10 \mu\text{m}$ to $20 \mu\text{m}$ depth from the surface. This means that target fragments are unlikely to be detected with FNTDs or PADCs due to their low fluence and short range, and consequently have a negligible impact on the assessed LET.

4.3.2. LET-to-medium with active detectors

The mini-TEPC enables tissue-equivalent measurements of \bar{y}_D through the use of tissue-equivalent materials for both the TEPC walls and the filling gas. This is not the case for the three other active detectors consisting of silicon, although the Timepix detector enables measurements with a sensitive gas volume. Silicon-based microdosimeters enable event-by-event based corrections from silicon to tissue or water if the ions stop completely within the relevant detector volume. When this is the case, the measurement of their energy enables a calculation of the energy deposition to the medium of interest through the stopping-power ratio of the two materials (Agosteo, 2022). For the silicon-telescope in Section 3.2, the range of 10 MeV protons in silicon corresponds to the thickness of the $500 \mu\text{m}$ thin E-stage, which enables single-event corrections for protons below that energy threshold. For ions with sufficient energy to cross the relevant detector structure, e.g. protons above 10 MeV for the silicon-telescope, the energy deposition to tissue can be approximated through the use of an average stopping-power ratio for the relevant particles and energies (Agosteo, 2022).

Silicon target fragmentation. When ion beams interact with silicon-based detectors, they have the potential to produce silicon fragments. As the silicon fragmentation spectrum differs from the spectra in water or tissue, the difference may impact the conversion from \bar{y}_D in silicon to \bar{y}_D in tissue or water. Although the effect of target fragmentation in silicon detectors is yet to be understood in detail, and may pose a challenge in certain situations, it is generally believed to constitute a small

effect with studies currently ongoing. Nevertheless, for system QA, the challenge of a different fragmentation spectrum can be overcome by utilizing the TPS to simulate \bar{y}_D to the detector material, e.g. silicon, instead of water or tissue.

Out-of-field measurements. For measurements outside the primary field, the conversion of LET from the detector medium to tissue is further complicated. Such measurements may be conducted to assess the dose of secondary particles or to measure clinical treatment plans with detectors that require a fluence or fluence-rate lower than in-field measurements permit to. Outside the primary field, the particle spectrum is dominated by neutrons, and their interactions with the detector is heavily influenced by its material composition, thus further complicating the assessment of dose and LET to water or tissue. However, detectors with a possibility to employ a particle discrimination, such as Timepix detectors, offer a possibility to filter particles through an LET-cutoff or by identifying nuclear interactions within the silicon sensor based on their characteristic signatures (Aricò et al., 2019; Burigo et al., 2020; Novak et al., 2023).

4.4. Radiation quality metrics different from LET

Although \bar{y}_D and $\overline{\text{LET}}_D$ remain the most frequently used radiation quality metrics in particle therapy, other metrics have historically been used to describe radiation fields. One of those is a metric closely related to the electronic stopper power, which models the detector response of an ion through z^{*2}/β^2 , where z^* is the effective charge of the particle and β its velocity relative to the speed of light in vacuum (Lühr et al., 2017; Kalholm et al., 2022). This metric is occasionally used in track structure theory and was originally conceived to describe the width of the ion track core in film emulsions (Barkas, 1963). Modeling radiobiological data with z^{*2}/β^2 , originally suggested by Folkard (1996), was recently suggested again to more accurately describe cell survival than with $\overline{\text{LET}}_D$ (Kalholm et al., 2022).

Extending the study by Kalholm et al. (2022), z^{*2}/β^2 was also found to provide a more accurate description of the radiation field than $\overline{\text{LET}}_F$ and $\overline{\text{LET}}_D$ for OSLDs irradiated in ion beams (Christensen et al., 2023). Although it highlights the fact that types of LET may not be the most suitable radiation quality metric, the challenges related to averaging of radiation quality metrics can be overcome with measurements of microdosimetric or particle spectra. However, modern treatment planning systems rely on LET and do not provide spectral information. This means, that the determination of $\overline{\text{LET}}_F$, and in particular $\overline{\text{LET}}_D$, remain the most popular metrics to validate treatment plans.

4.5. Spatial LET determinations

The majority of the detectors herein are only available for near point-like measurements, where the signal is averaged across a relatively small volume or surface area. For some of the passive luminescence detectors, the volume may span several mm^3 , which can pose

a challenge for measurements across steep $\overline{\text{LET}}$ gradients, e.g. across the distal edge of the spread-out Bragg peak region in particle therapy. Although the mini-TEPC provides quasi point-like measurements with an excellent resolution at a micrometer scale, sequential measurements are needed to map an entire spatial LET distribution. Such measurements are easier to conduct with the silicon telescope or the SOI Mushroom detector, which both enable pixelated measurements due to the use of SVs arranged in a matrix. Recently, [Guardiola et al. \(2023\)](#) demonstrated the ability to do two-dimensional microdosimetric measurements with a 200 μm resolution. In principle, spatial measurements are also possible with the passive TEDs and FNTDs although a variation of the radiation quality and LET across the detector volume affects the counting statistics. The active Timepix detector enables measuring LET maps with a spatial binning of 55 μm . Similarly, sub-millimeter pixelated measurements with OSLDs placed in an array have been demonstrated, although the reconstruction of the $\overline{\text{LET}}$ distribution requires extensive data management and organization ([Christensen et al., 2021](#)).

Nonetheless, with the increasing focus on the role of LET in particle therapy ([Mohan, 2022](#)), there is a need for mapping the spatial LET distribution with a sub-millimeter resolution, in particular for high-LET distributions near organs at risk. Although two-dimensional readers for OSLDs, RPLDs, and TLDs have been demonstrated for dosimetry with a sub-millimeter resolution ([Ahmed et al., 2014](#); [Nascimento et al., 2022](#); [Olko et al., 2006](#)), the readers have not been adapted to spatially resolved LET determinations yet.

4.6. LET-QA in particle therapy

For ions heavier than protons, clinical protocols very early implemented variable RBE models for carbon ions ([Jäkel et al., 2022](#)). For proton therapy, where RBE effects are possibly less pronounced, reports of toxicities at the distal edge of proton beams ([Mohan, 2022](#)) fuel the debate on whether current clinical practice of assuming $\text{RBE} = 1.1$ is justified, and emphasize the need for accurate TPS calculations of the LET, or another metric with predictive RBE capabilities.

Although $\overline{\text{LET}}_D$ is by far the most used metric to describe the radiation quality in proton therapy, the limitations of $\overline{\text{LET}}_D$ become increasingly evident when dealing with overlapping multiple fields that produce highly heterogeneous LET spectra. In such scenarios, $\overline{\text{LET}}_D$ may not accurately represent the observed biological effects ([Grün et al., 2019](#)). By contrast, microdosimetry-based RBE models operating with the entire measurable spectral information ([Kase et al., 2006](#); [Sato et al., 2021](#); [Parisi et al., 2022a](#)) offer a more elegant and potentially more accurate approach. Clinical LET-assessment may be an important tool to validate more complex plans, such as multi-ion therapy or LET-optimized plans, as discussed in [Inaniwa et al. \(2017\)](#) or recently in [Koto et al. \(2024\)](#).

Quality assurance in particle therapy involves the commissioning of the TPS, treatment machine, and patient-specific measurements ([Arjomandy et al., 2019](#)). Irrespective of the alternative suggested radiation quality metrics, $\overline{\text{LET}}_D$ remains a key metric in modern proton therapy centers, and therefore the validation of the TPS algorithm to calculate the LET distribution or spectra will constitute an essential part of clinical QA. Adding to the challenges related to $\overline{\text{LET}}_D$, a recent study demonstrated that the $\overline{\text{LET}}_D$ definition varies between proton therapy centers ([Hahn et al., 2022](#)) with respect to the use of particles and energy thresholds, which poses a challenge for experimental validations. It was, however, concluded that only minor discrepancies occurred between the centers once the LET definition was harmonized. That observation is in agreement with a systematic LET study, which emphasized how the colloquial use of LET has added to the uncertainty when reporting RBE, as often the underlying details of LET averaging are not described ([Kalholm et al., 2021](#)). Before administering LET optimized treatment to the first patient, a center is likely to ensure that the plans undergo rigorous patient-specific QA of the LET distribution

through end-to-end tests ([Wagenaar et al., 2020](#)). This means that the type of LET averaging needs to be carefully defined, or, perhaps, that the QA is conducted through measurements and simulations of spectra rather than $\overline{\text{LET}}$.

4.7. LET-QA detector requirements

The ideal QA of a TPS would involve simulation of the $\overline{\text{LET}}$ or microdosimetric spectra and measurements of such, where the detector would not disturb the radiation field being measured. For LET-QA without time constraints, e.g. a yearly QA of the TPS, postal audits would enable both independent validations and also help to maintain homogeneity in LET determination within proton therapy centers. For this purpose, passive luminescence detectors like OSLDs and TLDs are already commercially available and used for postal dose audits, which could be extended to include postal LET audits ([Carlino et al., 2021](#)). In a recent LET intercomparison for passive luminescence detectors, OSLDs, TLDs and FNTDs were demonstrated to correctly assess different types of $\overline{\text{LET}}$ as well as RBE in proton beams ([Muñoz et al., 2024b](#)). For LET-QA relevant to FLASH radiation conditions, dose-rate independent passive detectors could be employed ([Christensen et al., 2021](#)). For LET-QA within anthropomorphic phantoms, OSLDs have been demonstrated to assess $\overline{\text{LET}}$ in agreement with a TPS ([Bobić et al., 2024](#)) with a negligible disturbance of the radiation field. Such measurements with passive detectors are challenged by the delay between irradiations and post-processing, limiting their use for patient-specific LET-QA, which requires fast data acquisition and processing achievable only with an active detector. However, no commercially available active detector can currently assess the radiation quality at clinically relevant fluence rates for the energies relevant to ion beam therapy.

As a result, patient-specific LET-QA will continue to be conducted at a research level until a suitable detector is developed, while yearly LET-QA could theoretically begin now.

CRediT authorship contribution statement

Jeppe Brage Christensen: Writing – review & editing, Writing – original draft, Visualization, Software, Project administration, Methodology, Investigation, Formal analysis, Conceptualization. **Iván Domingo Muñoz:** Writing – review & editing, Writing – original draft. **Pawel Bilski:** Writing – review & editing, Writing – original draft, Methodology, Formal analysis. **Valeria Conte:** Writing – review & editing, Writing – original draft, Methodology. **Pawel Olko:** Writing – review & editing, Writing – original draft, Methodology, Formal analysis. **Lily Bossin:** Writing – review & editing, Writing – original draft, Methodology. **Anne Vestergaard:** Writing – review & editing, Writing – original draft. **Stefano Agosteo:** Writing – review & editing, Writing – original draft. **Anatoly Rosenfeld:** Writing – review & editing, Writing – original draft. **Linh Tran:** Writing – review & editing, Writing – original draft. **Željka Knežević:** Writing – review & editing, Writing – original draft. **Marija Majer:** Writing – review & editing, Writing – original draft. **Iva Ambrožová:** Writing – review & editing, Writing – original draft. **Alessio Parisi:** Writing – review & editing, Writing – original draft. **Tim Gehrke:** Writing – review & editing, Writing – original draft. **Mária Martišíková:** Writing – review & editing, Writing – original draft. **Niels Bassler:** Writing – review & editing, Writing – original draft, Methodology, Conceptualization.

Declaration of competing interest

The authors declare that they have no known competing financial interests or personal relationships that could have appeared to influence the work reported in this paper.

Data availability

No new data was used for the research described in the article.

Acknowledgments

The authors thank Dr. James Vohradsky (CMRP, UOW) for his help and advice on Monte Carlo simulations. The Polish contribution to this work was supported by National Science Centre (grant No. 2020/39/B/ST9/00459). I.D.M. acknowledges the German Academic Exchange Service for funding (program number: 57440921). T.G. was supported by Deutsche Forschungsgemeinschaft (DFG, German Research Foundation), Grant /AwardNumber: 426970603. The Croatian contribution was supported by Croatian Scientific Foundation (IP-2020-02-3593). N.B. is supported by the Novo Nordisk Foundation, Denmark (grant number NNF195A0059372), DCCC Radiotherapy — The Danish National Research Center for Radiotherapy, Danish Cancer Society (grant no. R191-A11526) and Danish Comprehensive Cancer Center.

References

- Abu Al Azm, S.M., Chelkov, G., Kozhevnikov, D., Guskov, A., Lapkin, A., Leyva Fabelo, A., Smolyanskiy, P., Zhemchugov, A., 2016. Response of timepix detector with GaAs:Cr and Si sensor to heavy ions. *Phys. Part. Nucl. Lett.* 13, 363–369.
- Agosteo, S., 2022. Detectors for measurement of microdosimetric quantities. *Radiat. Meas.* 156, 106807.
- Agosteo, S., Cirrone, G., Colautti, P., Cuttone, G., D'Angelo, G., Fazzi, A., Introini, M.V., Moro, D., Pola, A., Varoli, V., 2010. Study of a silicon telescope for solid state microdosimetry: Preliminary measurements at the therapeutic proton beam line of CATANA. *Radiat. Meas.* 45, 1284–1289.
- Agosteo, S., Cirrone, G., D'Angelo, G., Fazzi, A., Introini, M.V., Pola, A., 2011. Feasibility study of radiation quality assessment with a monolithic silicon telescope: Irradiations with 62 AMeV carbon ions at LNS-INFN. *Radiat. Meas.* 46, 1534–1538.
- Agosteo, S., Colautti, P., Fazzi, A., Moro, D., Pola, A., 2006. A solid state microdosimeter based on a monolithic silicon telescope. *Radiat. Prot. Dosim.* 122, 382–386.
- Agosteo, S., Fallica, P.G., Fazzi, A., Introini, M.V., Pola, A., Valvo, G., 2008. A pixelated silicon telescope for solid state microdosimetry. *Radiat. Meas.* 43, 585–589.
- Ahmed, M.F., Eller, S.A., Schnell, E., Ahmad, S., Akselrod, M.S., Hanson, O.D., Yukihiro, E.G., 2014. Development of a 2D dosimetry system based on the optically stimulated luminescence of Al_2O_3 . *Radiat. Meas.* 71, 187–192. <http://dx.doi.org/10.1016/j.radmeas.2014.01.009>.
- Akselrod, M.S., Akselrod, A.E., 2006. New Al_2O_3 :C, Mg crystals for radio-photoluminescent dosimetry and optical imaging. *Radiat. Prot. Dosim.* 119, 218–221.
- Akselrod, M.S., Akselrod, A.E., Orlov, S.S., Sanyal, S., Underwood, T.H., 2003. Fluorescent aluminum oxide crystals for volumetric optical data storage and imaging applications. *J. Fluorescence* 13, 503–511.
- Ambrožová, I., Brabcová, K.P., Kubancák, J., Šlegel, J., Toloček, R.V., Ivanova, O.A., Shurshakov, V.A., 2017. Cosmic radiation monitoring at low-Earth orbit by means of thermoluminescence and plastic nuclear track detectors. *Radiat. Meas.* 106, 262–266.
- Andreo, P., Burns, D.T., Nahum, A.E., Seuntjens, J., Attix, F.H., 2017. *Fundamentals of Ionizing Radiation Dosimetry*. John Wiley & Sons.
- Aricó, G., Gehrke, T., Gallas, R., Mairani, A., Jäkel, O., Martišková, M., 2019. Investigation of single carbon ion fragmentation in water and PMMA for hadron therapy. *Phys. Med. Biol.* 64, 055018.
- Arjomandy, B., Taylor, P., Ainsley, C., Safai, S., Sahoo, N., Pankuch, M., Farr, J.B., Yong Park, S., Klein, E., Flanz, J., et al., 2019. AAPM task group 224: Comprehensive proton therapy machine quality assurance. *Med. Phys.* 46, e678–e705.
- Bachiller-Perea, D., Zhang, M., Fleta, C., Quirion, D., Bassignana, D., Gómez, F., Guardiola, C., 2022. Microdosimetry performance of the first multi-arrays of 3D-cylindrical microdetectors. *Sci. Rep.* 12, 12240.
- Bahn, E., Bauer, J., Harrabi, S., Herfarth, K., Debus, J., Alber, M., 2020. Late contrast enhancing brain lesions in proton-treated patients with low-grade glioma: Clinical evidence for increased periventricular sensitivity and variable RBE. *Int. J. Radiat. Oncol. Biol. Phys.* 107, 571–578.
- Barkas, H.W., 1963. *Nuclear Research Emulsions*, vol. 1. Academic Press, New York and London.
- Bartz, J., Kodaira, S., Kurano, M., Yasuda, N., Akselrod, M., 2014. High resolution charge spectroscopy of heavy ions with FNTD technology. *Nucl. Instrum. Methods Phys. Res. B* 335, 24–30.
- Bassler, N., Jäkel, O., Søndergaard, C.S., Petersen, J.B., 2010. Dose-and LET-painting with particle therapy. *Acta Oncol.* 49, 1170–1176.
- Benton, E.R., Benton, E.V., 2001. Space radiation dosimetry in low-Earth orbit and beyond. *Nucl. Instrum. Methods Phys. Res. B* 184, 255–294. [http://dx.doi.org/10.1016/S0168-583X\(01\)00748-0](http://dx.doi.org/10.1016/S0168-583X(01)00748-0).
- Berger, T., Bilski, P., Hajek, M., Puchalska, M., Reitz, G., 2013. The MATROSHKA experiment: Results and comparison from extravehicular activity (MTR-1) and intravehicular activity (MTR-2A/2B) exposure. *Radiat. Res.* 180, 622–637.
- Berger, T., Burmeister, S., Matthiä, D., Przybyla, B., Reitz, G., Bilski, P., Hajek, M., Silver, L., Szabo, J., Ambrozova, I., et al., 2017. DOSIS & DOSIS 3D: Radiation measurements with the DOSTEL instruments onboard the columbus laboratory of the ISS in the years 2009–2016. *J. Space Weather Space Clim.* 7, A8.
- Berger, T., Hajek, M., Fugger, M., Vana, N., 2006. Efficiency-corrected dose verification with thermoluminescence dosimeters in heavy-ion beams. *Radiat. Prot. Dosim.* 120, 361–364.
- Bianchi, A., Selva, A., Colautti, P., Bortot, D., Mazzucconi, D., Pola, A., Agosteo, S., Petringa, G., Cirrone, G., Reniers, B., 2020. Microdosimetry with a sealed mini-TEPC and a silicon telescope at a clinical proton SOBP of CATANA. *Radiat. Phys. Chem.* 171, 108730.
- Bianchi, A., Selva, A., Colautti, P., Petringa, G., Cirrone, P., Reniers, B., Parisi, A., Vanhavere, F., Conte, V., 2021. Repeatability and reproducibility of microdosimetry with a mini-TEPC. *Front. Phys.* 9, 459.
- Bilski, P., 2006. Dosimetry of densely ionising radiation with three LiF phosphors for space applications. *Radiat. Prot. Dosim.* 120, 397–400.
- Bilski, P., 2010. On the correctness of the thermoluminescent high-temperature ratio (HTR) method for estimating ionisation density effects in mixed radiation fields. *Radiat. Meas.* 45, 42–50.
- Bilski, P., Marczevska, B., Gieszczyk, W., Klosowski, M., Naruszewicz, M., Sankowska, M., Kodaira, S., 2019. Fluorescent imaging of heavy charged particle tracks with LiF single crystals. *J. Lumin.* 213, 82–87.
- Bilski, P., Marczevska, B., Gieszczyk, W., Klosowski, M., Nowak, T., Naruszewicz, M., 2018. Lithium fluoride crystals as fluorescent nuclear track detectors. *Radiat. Prot. Dosim.* 178, 337–340.
- Bilski, P., Marczevska, B., Sankowska, M., Kilian, A., Swakoń, J., Siketić, Z., Olko, P., 2024. Detection of proton tracks with lif fluorescent nuclear track detectors. *Radiat. Meas.* 107083.
- Bilski, P., Matthiä, D., Berger, T., 2016. Influence of cosmic radiation spectrum and its variation on the relative efficiency of LiF thermoluminescent detectors – calculations and measurements. *Radiat. Meas.* 88, 33–40.
- Bobić, M., Christensen, J.B., Lee, H., Choulilitsa, E., Czerska, K., Togno, M., Safai, S., Yukihiro, E.G., Winey, B., Lomax, A., Paganetti, H., Albertini, F., Nesteruk, P., 2023. Optically stimulated luminescence dosimeters for simultaneous measurement of point dose and dose-weighted LET in an adaptive proton therapy workflow. *Front. Oncol. Radiat. Oncol.*
- Bobić, M., Christensen, J.B., Lee, H., Choulilitsa, E., Czerska, K., Togno, M., Safai, S., Yukihiro, E.G., Winey, B.A., Lomax, A.J., et al., 2024. Optically stimulated luminescence dosimeters for simultaneous measurement of point dose and dose-weighted LET in an adaptive proton therapy workflow. *Front. Oncol.* 13, 1333039.
- Bolzonella, M., Ambrožová, I., Caresana, M., Gibbens, N., Gilvin, P., Mariotti, F., Savary, A., Stabilini, A., Vittoria, F., Yukihiro, E., 2022. Neutron personal dosimetry using polyallyl diglycol carbonate (PADC): Current status, best practices and proposed research. *Phys. Open* 12, 100114.
- Brabcová, K.P., 2010. Study and Development of Track Etch Detectors for Dosimetric Purposes (Ph.D. thesis). Czech Technical University in Prague.
- Brabcová, K.P., Ambrožová, I., Kolísková, Z., Malušek, A., 2013. Uncertainties in linear energy transfer spectra measured with track-etched detectors in space. *Nucl. Instrum. Methods Phys. Res. A* 713, 5–10.
- Brabcová, K., Jadrnicková, I., Molokanov, A., Spurný, F., 2010. Dosimetry in heavy ion beams using various detectors. *Radiat. Meas.* 45, 1384–1386.
- Burigo, L., Gehrke, T., Jäkel, O., Sivertz, M., Olsen, T., Rusek, A., Obcemea, C., Greilich, S., 2020. Beam characterization at NSRL for radiobiological experiments — phase I. *J. Instrum.* 15.
- Cardella, G., Amorini, F., Cabibbo, M., Di Pietro, A., Fallica, G., Franzò, G., Figuera, P., Li, S., Musumarra, A., Papa, M., Pappalardo, G., Percolla, G., Priolo, F., Privitera, V., Rizzo, F., Tudisco, S., 1996. A monolithic silicon detector telescope. *Nucl. Instrum. Methods Phys. Res. A* 378, 262–266.
- Carlino, A., Palmans, H., Gouldstone, C., Trnkova, P., Noerrevang, O., Vestergaard, A., Freixas, G.V., Bosmans, G., Lorentini, S., Schwarz, M., et al., 2021. Results of an independent dosimetry audit for scanned proton beam therapy facilities. *Z. Med. Phys.* 31, 145–153.
- Chang, W., Koba, Y., Katayose, T., Yasui, K., Omachi, C., Hariu, M., Saitoh, H., 2017. Correction of stopping power and LET quenching for radiophotoluminescent glass dosimetry in a therapeutic proton beam. *Phys. Med. Biol.* 62, 8869–8881.
- Christensen, J.B., Muñoz, I.D., Bassler, N., Stengl, C., Bossin, L., Togno, M., Safai, S., Jäkel, O., Yukihiro, E.G., 2023. Optically stimulated luminescence detectors for dosimetry and LET measurements in light-ion beams. *Phys. Med. Biol.* 68, 155001.
- Christensen, J.B., Togno, M., Bossin, L., Pakari, O.V., Safai, S., Yukihiro, E.G., 2022. Improved simultaneous LET and dose measurements in proton therapy. *Sci. Rep.* 12, 1–10.
- Christensen, J.B., Togno, M., Nesteruk, K.P., Psoroulas, S., Meer, D., Weber, D.C., Lomax, T., Yukihiro, E.G., Safai, S., 2021. Al_2O_3 :C optically stimulated luminescence dosimeters (OSLDs) for ultra-high dose rate proton dosimetry. *Phys. Med. Biol.* 66.
- Ciesielski, B., Stuglik, Z., Wielopolski, L., Zvara, I., 1998. The effect of high-linear energy transfer ions on the electron paramagnetic resonance signal induced in alanine. *Radiat. Res.* 150, 469–474.
- Ciesielski, B., Wielopolski, L., 1994. The effects of dose and radiation quality on the shape and power saturation of the EPR signal in alanine. *Radiat. Res.* 140, 105–111.

- Colautti, P., Bianchi, A., Selva, A., Bortot, D., Mazzucconi, D., Pola, A., Agosteo, S., Petringa, G., Cirrone, G., Conte, V., 2020. Therapeutic proton beams: LET, RBE and microdosimetric spectra with gas and silicon detectors. *Radiat. Meas.* 136, 106386.
- Colautti, P., Conte, V., Selva, A., Chiriotti, S., Pola, A., Bortot, D., Fazzi, A., Agosteo, S., Ciocca, M., 2018a. Microdosimetric study at the CNAO active-scanning carbon-ion beam. *Radiat. Prot. Dosim.* 180, 157–161.
- Colautti, P., Conte, V., Selva, A., Chiriotti, S., Pola, A., Bortot, D., Fazzi, A., Agosteo, S., Treccani, M., De Nardo, L., 2018b. Miniaturized microdosimeters as LET monitors: First comparison of calculated and experimental data performed at the 62 MeV/u 12C beam of INFN-LNS with four different detectors. *Phys. Medica* 52, 113–121.
- Conte, V., Agosteo, S., Bianchi, A., Bolst, D., Bortot, D., Catalano, R., Cirrone, G.A.P., Colautti, P., Cuttone, G., Guatelli, S., James, B., Mazzucconi, D., Rosenfeld, A.B., Selva, A., Tran, L., Petringa, G., 2020. Microdosimetry of a therapeutic proton beam with a mini-TEPC and a MicroPlus-bridge detector for RBE assessment. *Phys. Med. Biol.* 65.
- Conte, V., Bianchi, A., Selva, A., Petringa, G., Cirrone, G., Parisi, A., Vanhavere, F., Colautti, P., 2019. Microdosimetry at the CATANA 62 MeV proton beam with a sealed miniaturized TEPC. *Phys. Medica* 64, 114–122.
- Cortés-Giraldo, M.A., Carabe, A., 2015. A critical study of different Monte Carlo scoring methods of dose average linear-energy-transfer maps calculated in voxelized geometries irradiated with clinical proton beams. *Phys. Med. Biol.* 60, 2645–2669.
- De Nardo, L., Cesari, V., Donà, G., Magrin, G., Colautti, P., Conte, V., Tornielli, G., 2004. Mini-TEPCs for radiation therapy. *Radiat. Prot. Dosim.* 108, 345–352.
- De Saint-Hubert, M., Castellano, F., Leblans, P., Sterckx, P., Kodaira, S., Swakon, J., de Freitas Nascimento, L., 2021. Characterization of 2D Al₂O₃:C, Mg radiophotoluminescence films in charged particle beams. *Radiat. Meas.* 141.
- Durrani, S.A., Bull, R.K., 1987. *Solid State Nuclear Track Detection: Principles, Methods and Applications*. Pergamon Ex Press, Oxford, New York.
- Edmund, J.M., Andersen, C.E., Greilich, S., 2007. A track structure model of optically stimulated luminescence from Al₂O₃:C irradiated with 10–60 MeV protons. *Nucl. Instrum. Methods Phys. Res. B* 262, 261–275.
- Eulitz, J., Troost, E.G., Klünder, L., Raschke, F., Hahn, C., Schulz, E., Seidlitz, A., Thiem, J., Karpowitz, C., Hahlbohm, P., et al., 2023. Increased relative biological effectiveness and periventricular radiosensitivity in proton therapy of glioma patients. *Radiother. Oncol.* 178, 109422.
- Félix-Bautista, R., Hamad, Y., Yáñez González, T., Ochoa-Parra, P., Granja, C., Martišková, M., Mairani, A., Gehrke, T., 2024. Towards precise LET measurements based on energy deposition of therapeutic ions in Timepix3 detectors. *Phys. Med. Biol.* 69, 125030.
- Fleisher, R., Price, P., Walker, R., 1975. *Nuclear Tracks in Solids: Principles and Applications*. Berkeley.
- Folkard, M., 1996. Inactivation of V79 cells by low-energy protons, deuterons and helium-3 ions. *Int. J. Radiat. Biol.* 69, 729–738.
- Friedrich, T., Scholz, U., Elsässer, T., Durante, M., Scholz, M., 2013. Systematic analysis of RBE and related quantities using a database of cell survival experiments with ion beam irradiation. *J. Radiat. Res.* 54, 494–514.
- Gehrke, T., Burigo, L., Aricó, G., Berke, S., Jakubek, J., Turecek, D., Tessonier, T., Mairani, A., Martišková, M., 2017. Energy deposition measurements of single 1H, 4He and 12C ions of therapeutic energies in a silicon pixel detector. *J. Instrum.* 12, P04025.
- George, S., Kroupa, M., Wheeler, S., Kodaira, S., Kitamura, H., Tlustos, L., Campbell-Ricketts, T., Stoffle, N., Semones, E., Pinsky, L., 2018. Very high energy calibration of silicon timepix detectors. *J. Instrum.* 13, P11014.
- Granja, C., Jakubek, J., Köster, U., Platteck, M., Pospisil, S., 2011. Response of the pixel detector Timepix to heavy ions. *Nucl. Instrum. Methods Phys. Res. A* 633, S198–S202.
- Granja, C., Jakubek, J., Polansky, S., Zach, V., Krist, P., Chvatil, D., Stursa, J., Sommer, M., Ploc, O., Kodaira, S., 2018. Resolving power of pixel detector timepix for wide-range electron, proton and ion detection. *Nucl. Instrum. Methods Phys. Res. A* 908, 60–71.
- Granja, C., Oancea, C., Jakubek, J., Marek, L., Benton, E., Kodaira, S., Miller, J., Rucinski, A., Gajewski, J., Stasica, P., 2021. Wide-range tracking and LET-spectra of energetic light and heavy charged particles. *Nucl. Instrum. Methods Phys. Res. A* 988, 164901.
- Granville, D.A., Sahoo, N., Sawakuchi, G.O., 2014a. Calibration of the Al₂O₃:C optically stimulated luminescence (OSL) signal for linear energy transfer (LET) measurements in therapeutic proton beams. *Phys. Med. Biol.* 59, 4295–4310.
- Granville, D.A., Sahoo, N., Sawakuchi, G.O., 2014b. Linear energy transfer dependence of Al₂O₃:C optically stimulated luminescence detectors exposed to therapeutic proton beams. *Radiat. Meas.* 71, 69–73.
- Granville, D.A., Sahoo, N., Sawakuchi, G.O., 2016. Simultaneous measurements of absorbed dose and linear energy transfer in therapeutic proton beams. *Phys. Med. Biol.* 61, 1765–1779.
- Greilich, S., Osinga, J.M., Niklas, M., Lauer, F.M., Klimpki, G., Bestvater, F., Bartz, J.A., Akseled, M.S., Jäkel, O., 2013. Fluorescent nuclear track detectors as a tool for ion-beam therapy research. *Radiat. Meas.* 56, 267–272.
- Grün, R., Friedrich, T., Traneus, E., Scholz, M., 2019. Is the dose-averaged LET a reliable predictor for the relative biological effectiveness? *Med. Phys.* 46, 1064–1074.
- Grzanka, L., Ardenfors, O., Bassler, N., 2018. Monte Carlo simulations of spatial LET distributions in clinical proton beams. *Radiat. Prot. Dosim.* 180, 296–299.
- Guardiola, C., Bachiller-Perea, D., Kole, E.M.M., Fleta, C., Quirion, D., De Marzi, L., Gómez, F., 2023. First experimental measurements of 2D microdosimetry maps in proton therapy. *Med. Phys.* 50, 570–581.
- Gustafsson, H., Lund, A., Lund, E., 2011. Potassium dithionate EPR dosimetry for determination of absorbed dose and LET distributions in different radiation qualities. *Radiat. Meas.* 46, 936–940.
- Hahn, C., Öden, J., Dasu, A., Vestergaard, A., Fuglsang Jensen, M., Sokol, O., Pardi, C., Bourhaleb, F., Leite, A., de Marzi, L., Smith, E., Aitkenhead, A., Rose, C., Merchant, M., Kirkby, K., Grzanka, L., Pawelke, J., Lühr, A., 2022. Towards harmonizing clinical linear energy transfer (LET) reporting in proton radiotherapy: A European multi-centric study. *Acta Oncol.* 61, 206–214.
- Hajek, M., Berger, T., Bergmann, R., Vana, N., Uchihori, Y., Yasuda, N., Kitamura, H., 2008. LET dependence of thermoluminescent efficiency and peak height ratio of CaF₂:Tm. *Radiat. Meas.* 43, 1135–1139.
- Hansen, J.W., Olsen, K., 1985. Theoretical and experimental radiation effectiveness of the free radical dosimeter alanine to irradiation with heavy charged particles. *Radiat. Res.* 104, 15–27.
- Harrabi, S.B., Nettelbladt, B.von., Gudden, C., Adeberg, S., Seidensaal, K., Bauer, J., Bahn, E., Mairani, A., Alber, M., Haberer, T., et al., 2022. Radiation induced contrast enhancement after proton beam therapy in patients with low grade glioma—how safe are protons? *Radiother. Oncol.* 167, 211–218.
- Hayashi, T., Doke, T., Kikuchi, J., Takeuchi, R., Hasebe, N., Ogura, K., Nagaoka, S., Kato, M., Badhwar, G.D., 1996. Measurement of LET distribution and dose equivalent on board the space shuttle STS-65. *Radiat. Meas.* 26, 935–945.
- Hirano, Y., Kodaira, S., Souda, H., Matsumura, A., Torikoshi, M., 2018. Linear energy transfer (LET) spectra and survival fraction distribution based on the CR-39 plastic charged-particle detector in a spread-out Bragg peak irradiation by a¹²C beam. *Phys. Med. Biol.* 63, 185006.
- Hirata, Y., Sato, T., Watanabe, K., Ogawa, T., Parisi, A., Uritani, A., 2022. Theoretical and experimental estimation of the relative optically stimulated luminescence efficiency of an optical-fiber-based BaFBr:Eu detector for swift ions.
- Hoffmann, W., Moller, G., 1980. Heavy particle dosimetry with high temperature peaks of thermoluminescent materials. *Nucl. Instrum. Methods* 175, 205–207.
- ICRP, 2013. *Assessment of Radiation Exposure of Astronauts in Space*. Report 123.
- ICRU, 1970. *Linear Energy Transfer*. Report 16.
- Inaniwa, T., Kanematsu, N., Noda, K., Kamada, T., 2017. Treatment planning of intensity modulated composite particle therapy with dose and linear energy transfer optimization. *Phys. Med. Biol.* 62, 5180.
- Jäkel, O., Kraft, G., Karger, C.P., 2022. The history of ion beam therapy in Germany. *Z. Med. Phys.* 32, 6–22.
- Jakubek, J., 2011. Precise energy calibration of pixel detector working in time-over-threshold mode. *Nucl. Instrum. Methods Phys. Res. A* 633, S262–S266.
- James, B., Tran, L.T., Bolst, D., Peracchi, S., Davis, J.A., Prokopovich, D.A., Guatelli, S., Petasecca, M., Lerch, M., Povoli, M., et al., 2019. SOI thin microdosimeters for high LET single-event upset studies in Fe, O, Xe, and cocktail ion beam fields. *IEEE Trans. Nucl. Sci.* 67, 146–153.
- Johnson, C., Benton, E., Yasuda, N., Benton, E., 2009. Analysis of short-range tracks and large track fluences in CR-39 PNTD using atomic force microscopy. *Radiat. Meas.* 44, 742–745.
- Kalholm, F., Grzanka, L., Toma-Dasu, I., Bassler, N., 2022. Modeling RBE with other quantities than LET significantly improves prediction of in vitro cell survival for proton therapy. *Med. Phys.* 50, 651–659.
- Kalholm, F., Grzanka, L., Traneus, E., Bassler, N., 2021. A systematic review on the usage of averaged LET in radiation biology for particle therapy. *Radiother. Oncol.* 161, 211–221.
- Kanai, T., Furusawa, Y., Fukutsu, K., Itsuikaichi, H., Eguchi-Kasai, K., Ohara, H., 1997. Irradiation of mixed beam and design of spread-out Bragg peak for heavy-ion radiotherapy. *Radiat. Res.* 147, 78–85.
- Karger, C.P., Glowa, C., Peshcke, P., Kraft-Weyrather, W., 2021. The RBE in ion beam radiotherapy: In vivo studies and clinical application. *Z. Med. Phys.* 31, 105–121.
- Karsch, L., Beyreuther, E., Burris-Mog, T., Kraft, S., Richter, C., Zeil, K., Pawelke, J., 2012. Dose rate dependence for different dosimeters and detectors: TLD, OSL, EBT films, and diamond detectors. *Med. Phys.* 39, 2447–2455.
- Kase, Y., Kanai, T., Matsumoto, Y., Furusawa, Y., Okamoto, H., Asaba, T., Sakama, M., Shinoda, H., 2006. Microdosimetric measurements and estimation of human cell survival for heavy-ion beams. *Radiat. Res.* 166, 629–638.
- Kellerer, A.M., 1985. *Fundamentals of Microdosimetry*, vol. I. Academic Press, Inc.
- Klikauga, P., 1994. Nanodosimetry of heavy ions using a miniature cylindrical counter of wall-less design. *Radiat. Prot. Dosim.* 52, 317–321.
- Klimpki, G., Mescher, H., Akseled, M.S., Jäkel, O., Greilich, S., 2016. Fluence-based dosimetry of proton and heavier ion beams using single track detectors. *Phys. Med. Biol.* 61, 1021–1040.
- Knoll, G.F., 2010. *Radiation Detection and Measurement*, third ed. John Wiley & Sons.
- Kodaira, S., Kitamura, H., Kurano, M., Kawashima, H., Benton, E.R., 2019. Contribution to dose in healthy tissue from secondary target fragments in therapeutic proton, He and C beams measured with CR-39 plastic nuclear track detectors. *Sci. Rep.* 9, 3708.
- Kodaira, S., Konishi, T., Kitamura, H., Kurano, M., Kawashima, H., Uchihori, Y., Nishio, T., Yasuda, N., Ogura, K., Sihver, L., et al., 2015. On the use of CR-39 PNTD with AFM analysis in measuring proton-induced target fragmentation particles. *Nucl. Instrum. Methods Phys. Res. B* 349, 163–168.

- Kodaira, S., Kusumoto, T., Kitamura, H., Yanagida, Y., Koguchi, Y., 2020. Characteristics of fluorescent nuclear track detection with Ag⁺-activated phosphate glass. *Radiat. Meas.* 132, 106252.
- Kodaira, S., Yasuda, N., Konishi, T., Kitamura, H., Kurano, M., Kawashima, H., Uchihoji, Y., Ogura, K., Benton, E., 2013. Calibration of CR-39 with atomic force microscope for the measurement of short range tracks from proton-induced target fragmentation reactions. *Radiat. Meas.* 50, 232–236.
- Koto, M., Ikawa, H., Inaniwa, T., Imai, R., Shinoto, M., Takiyama, H., Isozaki, T., Mizuno, H., Kohno, R., Takahashi, I., Yoshida, N., Yamada, S., 2024. Dose-averaged LET optimized carbon-ion radiotherapy for head and neck cancers. *Radiother. Oncol.* 194, 110180.
- Krushev, V.V., Koizumi, H., Ichikawa, T., Yoshida, H., Shibata, H., Tagawa, S., Yoshida, Y., 1994. Relation between track structure and LET effect on free radical formation for ion beam-irradiated alanine dosimeter. *Radiat. Phys. Chem.* 44, 521–526.
- Kusumoto, T., Akselrod, M.S., Harrison, J., Kodaira, S., 2023. Correction method of the coloration in fluorescent nuclear track detector. *Radiat. Meas.* 161, 106898.
- Leidner, J., Murtas, F., Silari, M., 2021. Medical applications of the GEMPix. *Appl. Sci.* 11, 440.
- Llopart, X., Aloyo, J., Ballabriga, R., Campbell, M., Casanova, R., Gromov, V., Heijne, E., Poikela, T., Santin, E., Sriskaran, V., 2022. Timepix4, a large area pixel detector readout chip which can be tiled on 4 sides providing sub-200 ps timestamp binning. *J. Instrum.* 17, C01044.
- Llopart, X., Ballabriga, R., Campbell, M., Tlustos, L., Wong, W., 2007. Timepix, a 65k programmable pixel readout chip for arrival time, energy and/or photon counting measurements. *Nucl. Instrum. Methods Phys. Res. A* 581, 485–494.
- Lühr, A., von Neubeck, C., Helmbrecht, S., Baumann, M., Enghardt, W., Krause, M., 2017. Modeling in vivo relative biological effectiveness in particle therapy for clinically relevant endpoints. *Acta Oncol.* 56, 1392–1398.
- Magrin, G., Palmans, H., Stock, M., Georg, D., 2023. State-of-the-art and potential of experimental microdosimetry in ion-beam therapy. *Radiother. Oncol.* 109586.
- Majer, M., Pasariček, L., Knežević, v., Bokulic, T., Provatas, G., Mihalic, I.B., 2023. Relative efficiency of radiophotoluminescent glass detectors in low energy ion beams. *Radiat. Meas.* 106973.
- Malinen, E., 2014. EPR dosimetry in clinical applications. In: *Applications of EPR in Radiation Research*. pp. 509–538.
- Marrale, M., Brai, M., Triolo, A., Bartolotta, A., D'Oca, M.C., 2006. Power saturation of ESR signal in ammonium tartrate exposed to ⁶⁰Co γ -ray photons, electrons and protons. *Radiat. Res.* 166, 802–809.
- Marrale, M., Longo, A., Brai, M., Barbon, A., Brustolon, M., 2014. Discrimination of radiation quality through second harmonic out-of-phase CW-ESR detection. *Rad. Res.* 181, 184–192.
- McKeever, S., Yukihara, E.G., 2011. *Optically Stimulated Luminescence: Fundamentals and Applications*. John Wiley & Sons, p. 388.
- Miyamoto, Y., Nanto, H., Kurobori, T., Fujimoto, Y., Yanagida, T., Ueda, J., Tanabe, S., Yamamoto, T., 2014. RPL in alpha particle irradiated Ag⁺-doped phosphate glass. *Radiat. Meas.* 71, 529–532.
- Mohan, R., 2022. A review of proton therapy—current status and future directions. *Precis. Radiat. Oncol.* 6, 164–176.
- Motta, S., Christensen, J.B., Frei, F., Peier, P., Yukihara, E.G., 2023a. Investigation of TL and OSL detectors in ultra-high dose rate electron beams. *Phys. Med. Biol.* 68, 145007.
- Motta, S., Christensen, J.B., Togno, M., Schäfer, R., Safai, S., Lomax, A.J., Yukihara, E.G., 2023b. Characterization of LiF: Mg, Ti thermoluminescence detectors in low-LET proton beams at ultra-high dose rates. *Phys. Med. Biol.* 68, 045017.
- Muñoz, I.D., Burigo, L.N., Gehrke, T., Brons, S., Greilich, S., Jäkel, O., 2022. Sensitivity correction of fluorescent nuclear track detectors using alpha particles: Determining LET spectra of light ions with enhanced accuracy. *Med. Phys.* 50, 2385–2401.
- Muñoz, I.D., GarcíaCalderón, D., FelixBautista, R., Burigo, L.N., Christensen, J.B., Brons, S., Runz, A., Häring, P., Greilich, S., Seco, J., et al., 2024a. Linear energy transfer measurements and estimation of relative biological effectiveness in proton and helium-ion beams using fluorescent nuclear track detectors. *Int. J. Radiat. Oncol. Biol. Phys.*
- Muñoz, I.D., van Hoey, O., Parisi, A., Bassler, N., Grzanka, N., de Saint-Hubert, M., Vaniqui, A., Olko, P., Sadel, M., Stolarczyk, L., Vestergaard, A., Jäkel, O., Yukihara, E.G., Christensen, J.B., 2024b. Assessment of fluence- and dose-averaged linear energy transfer with passive luminescence detectors in clinical proton beams. *Phys. Med. Biol.* 69, 135004.
- Nabha, R., Van Hoey, O., Granja, C., Parisi, A., Saint-De Hubert, M., Struelens, L., Oancea, C., Sterpin, E., Zach, V., Stursa, J., Rucinski, A., Gajewski, J., Stastica, P., Vanhavere, F., 2022. A novel method to assess the incident angle and the LET of protons using a compact single-layer Timepix detector. *Radiat. Phys. Chem.* 199, 110349.
- Nakagawa, K., Ikota, N., Sato, Y., 2008. Heavy-ion-induced sucrose and L- α -alanine radicals investigated by EPR. *Appl. Magn. Reson.* 33, 111–116.
- Nakaji, T., Kanai, T., Takashina, M., Matsumura, A., Osaki, K., Yagi, M., Tsubouchi, T., Hamatani, N., Ogawa, K., 2022. Clinical dose assessment for scanned carbon-ion radiotherapy using linear energy transfer measurements and Monte Carlo simulations. *Phys. Med. Biol.* 67, 245021.
- Nascimento, L., Leblans, P., van der Heyden, B., Akselrod, M., Goossens, J., Verellen, D., Kodaira, S., 2022. Characterization and quenching correction for a 2D real time radioluminescent system in therapeutic proton and carbon charged beams. *Sensors Actuators A* 345, 113781.
- Novak, A., Granja, C., Sagatova, A., Zach, V., Stursa, J., Oancea, C., 2023. Spectral tracking of proton beams by the Timepix3 detector with GaAs, CdTe and Si sensors. *Jour. Instrum.* 18, C01022.
- Oancea, C., Ambrožová, I., Popescu, A., Mytsin, G., Vondráček, V., Davidková, M., 2018. LET spectra behind high-density titanium and stainless steel hip implants irradiated with a therapeutic proton beam. *Radiat. Meas.* 110, 7–13.
- Oancea, C., Granja, C., Marek, L., Jakubek, J., Šlc, J., Bodenstern, E., Gantz, S., Pawelke, J., Pivec, J., 2023. Out-of-field measurements and simulations of a proton pencil beam in a wide range of dose rates using a Timepix3 detector: Dose rate, flux and LET. *Phys. Medica* 106, 102529.
- Olko, P., Bilski, P., 2021. Microdosimetric understanding of dose response and relative efficiency of thermoluminescence detectors. *Radiat. Prot. Dosim.* 192, 165–177.
- Olko, P., Bilski, P., Budzanowski, M., Patrick, M., Waligórski, R., Reitz, G., 2002. Modeling the response of thermoluminescence detectors exposed to low- and high-LET radiation fields. *J. Radiat. Res.* 43, 59–62.
- Olko, P., Marczewska, B., Czopyk, L., Czermak, M., Kłowski, M., Waligórski, M.P.R., 2006. New 2-D dosimetric technique for radiotherapy based on planar thermoluminescent detectors. *Radiat. Prot. Dosim.* 118, 213–218.
- Osinga, J.M., Ambrožová, I., Brabcová, K.P., Akselrod, M.S., Jäkel, O., Davidková, M., Greilich, S., 2014. Single track coincidence measurements of fluorescent and plastic nuclear track detectors in therapeutic carbon beams. *J. Instrum.* 9, P04013.
- Parisi, A., Beltran, C.J., Furutani, K.M., 2022a. The mayo clinic florida microdosimetric kinetic model of clonogenic survival: Formalism and first benchmark against in vitro and in silico data. *Phys. Med. Biol.* 67, 185013.
- Parisi, A., Chiriotti, S., De Saint-Hubert, M., Van Hoey, O., Vandevoorde, C., Beukes, P., de Kock, E.A., Symons, J., Camero, J.N., Slabbert, J., et al., 2019a. A novel methodology to assess linear energy transfer and relative biological effectiveness in proton therapy using pairs of differently doped thermoluminescent detectors. *Phys. Med. Biol.* 64, 085005.
- Parisi, A., Olko, P., Swakoń, J., Horwacik, T., Jabłoński, H., Malinowski, L., Nowak, T., Struelens, L., Vanhavere, F., 2020. Modeling the radiation-induced cell death in a therapeutic proton beam using thermoluminescent detectors and radiation transport simulations. *Phys. Med. Biol.* 65, 015008.
- Parisi, A., Olko, P., Swakon, J., Horwacik, T., Jablonski, H., Malinowski, L., Nowak, T., Struelens, L., Vanhavere, F., 2022b. Microdosimetric characterization of a clinical proton therapy beam: Comparison between simulated lineal energy distributions in spherical water targets and experimental measurements with a silicon detector. *Phys. Med. Biol.* 67, 015006.
- Parisi, G., Romano, F., Schettino, G., 2022c. Microdosimetry for hadron therapy: A state of the art of detection technology. *Front. Phys.* 10, 1035956.
- Parisi, A., Van Hoey, O., Mégret, P., Vanhavere, F., 2019b. Microdosimetric specific energy probability distribution in nanometric targets and its correlation with the efficiency of thermoluminescent detectors exposed to charged particles. *Radiat. Meas.* 123, 1–12.
- Petringa, G., Pandola, L., Agosteo, S., Catalano, R., Colautti, P., Conte, V., Cuttone, G., Fan, K., Mei, Z., Rosenfeld, A., 2020. Monte Carlo implementation of new algorithms for the evaluation of averaged-dose and-track linear energy transfers in 62 MeV clinical proton beams. *Phys. Med. Biol.* 65, 235043.
- Ploc, O., Sommer, M., Kakona, M., Kubancak, J., Peksova, D., Molokanov, A., Sihver, L., 2018. Intercomparison of LET Spectra Measured with Timepix and TEPC in Reference Radiation Field CERF. *IEEE*.
- Rørvik, E., Fjæra, L.F., Dahle, T.J., Dale, J.E., Engeseth, G.M., Stokkevåg, C.H., Thörnqvist, S., Ytre-Hauge, K.S., 2018. Exploration and application of phenomenological RBE models for proton therapy. *Phys. Med. Biol.* 63, 185013.
- Rosenfeld, A.B., 2016. Novel detectors for silicon based microdosimetry, their concepts and applications. *Nucl. Instrum. Methods Phys. Res. A* 809, 156–170.
- Rossi, H.H., 1959. Specification of radiation quality. *Radiat. Res.* 10, 522–531.
- Rossi, H.H., Rosenzweig, W., 1955. A device for the measurement of dose as a function of specific ionization. *Radiology* 64, 404–411.
- Sadel, M., Bilski, P., Swakon, J., Rydygier, M., Horwacik, T., Weber, A., 2015. Comparative investigations of the relative thermoluminescent efficiency of LiF detectors to protons at different proton therapy facilities. *Radiat. Meas.* 82, 8–13.
- Sakama, M., Kanai, T., Kase, Y., Yusa, K., Tashiro, M., Torikai, K., Shimada, H., Yamada, S., Ohno, T., Nakano, T., 2012. Design of ridge filters for spread-out Bragg peaks with Monte Carlo simulation in carbon ion therapy. *Phys. Med. Biol.* 57, 6615.
- Sato, T., Hashimoto, S., Inaniwa, T., Takada, K., Kumada, H., 2021. Implementation of simplified stochastic microdosimetric kinetic models into PHITS for application to radiation treatment planning. *Int. J. Radiat. Biol.* 97, 1450–1460.
- Sawakuchi, G., Sahoo, N., Gasparian, P., Rodriguez, M., Archambault, L., Titt, U., Yukihara, E., 2010. Determination of average LET of therapeutic proton beams using Al₂O₃:C optically stimulated luminescence (OSL) detectors. *Med. Phys.* 37, 3453.

- Sawakuchi, G.O., Yukihiro, E., McKeever, S., Benton, E., Gaza, R., Uchihori, Y., Yasuda, N., Kitamura, H., 2008. Relative optically stimulated luminescence and thermoluminescence efficiencies of $\text{Al}_2\text{O}_3:\text{C}$ dosimeters to heavy charged particles with energies relevant to space and radiotherapy dosimetry. *J. Appl. Phys.* 104, 124903.
- Scholz, M., Kraft, G., 1996. Track structure and the calculation of biological effects of heavy charged particles. *Adv. Space Res.* 18, 5–14.
- Sholom, S., McKeever, S., 2023. Silver molecular clusters and the properties of radiophotoluminescence of alkali-phosphate glasses at high dose. *Radiat. Meas.* 163, 106924.
- Šolc, J., Jakubek, J., Marek, L., Oancea, C., Pivec, J., Šmoldasová, J., Tesař, J., Vykýdal, Z., 2022. Monte Carlo modelling of pixel clusters in Timepix detectors using the MCNP code. *Phys. Medica* 101, 79–86.
- Sommer, M., Granja, C., Kodaira, S., Ploc, O., 2022. High-energy per-pixel calibration of timepix pixel detector with laboratory alpha source. *Nucl. Instrum. Methods Phys. Res. A* 1022, 165957.
- Stasica, P., Nguyen, H., Granja, C., Kopec, R., Marek, L., Oancea, C., Raczynski, L., Rucinski, A., Rydygier, M., Schubert, K.E., 2023. Single proton LET characterization with the Timepix detector and artificial intelligence for advanced proton therapy treatment planning. *Phys. Med. Biol.* 68, 104001.
- Stoffle, N., Pinsky, L., Kroupa, M., Hoang, S., Idarraga, J., Amberboy, C., Rios, R., Hauss, J., Keller, J., Bahadori, A., 2015. Timepix-based radiation environment monitor measurements aboard the international space station. *Nucl. Instrum. Methods Phys. Res. A* 782, 143–148.
- Sykora, G.J., Akselrod, M.S., Benton, E.R., Yasuda, N., 2008. Spectroscopic properties of novel fluorescent nuclear track detectors for high and low LET charged particles. *Radiat. Meas.* 43, 422–426.
- Tran, L.T., Bolst, D., James, B., Pan, V., Vohradsky, J., Peracchi, S., Chartier, L., Debrot, E., Guatelli, S., Petasecca, M., Lerch, M., Prokopovich, D., Povoli, M., Kok, A., Inaniwa, T., Lee, S.H., Matsufuji, N., Rosenfeld, A.B., 2021. Silicon 3D microdosimeters for advanced quality assurance in particle therapy. *Appl. Sci.* 12, 328.
- Tran, L.T., Chartier, L., Bolst, D., Pogossov, A., Guatelli, S., Petasecca, M., Lerch, M.L., Prokopovich, D.A., Reinhard, M.I., Clasié, B., et al., 2017. Characterization of proton pencil beam scanning and passive beam using a high spatial resolution solid-state microdosimeter. *Med. Phys.* 44, 6085–6095.
- Turecek, D., Jakubek, J., Soukup, P., 2016. USB 3.0 readout and time-walk correction method for Timepix3 detector. *J. Instrum.* 11, C12065.
- Unkelbach, J., Botas, P., Giantsoudi, D., Gorissen, B.L., Paganetti, H., 2016. Reoptimization of intensity modulated proton therapy plans based on linear energy transfer. *Int. J. Radiat. Oncol. Biol. Phys.* 96, 1097–1106.
- Vana, N., Schöne, W., Fugger, M., Akatov, Y., 1996. Absorbed dose measurement and LET determination with TLDs in space. *Radiat. Prot. Dosim.* 66, 145–152.
- Vanhavere, F., Genicot, J.L., O'Sullivan, D., Zhou, D., Spurný, F., Jadrníčková, I., Sawakuchi, G.O., Yukihiro, E.G., 2008. Dosimetry of biological experiments in Space (DOBIES) with luminescence (OSL and TL) and track etch detectors. *Radiat. Meas.* 43, 694–697.
- Vedelago, J., Karger, C., Jäkel, O., 2022. A review on reference dosimetry in radiation therapy with proton and light ion beams: Status and impact of new developments. *Radiat. Meas.* 157, 106844.
- Verkhovtsev, A., Zimmer, L., Greilich, S., 2019. Calibration of intensity spectra from fluorescent nuclear track detectors in clinical ion beams. *Radiat. Meas.* 121, 37–41.
- Wagenaar, D., Tran, L.T., Meijers, A., Marmitt, G.G., Souris, K., Bolst, D., James, B., Biasi, G., Povoli, M., Kok, A., Traneus, E., Van Goethem, M.J., Langendijk, J.A., Rosenfeld, A.B., Both, S., 2020. Validation of linear energy transfer computed in a Monte Carlo dose engine of a commercial treatment planning system. *Phys. Med. Biol.* 65, 025006.
- Waldeland, E., Hole, E.O., Stenerlöw, B., Grusell, E., Sagstuen, E., Malinen, E., 2010. Radical formation in lithium formate EPR dosimeters after irradiation with protons and nitrogen ions. *Radiat. Res.* 174, 251–257.
- Wilkens, J.J., Oelfke, U., 2003. Analytical linear energy transfer calculations for proton therapy. *Med. Phys.* 30, 806–815.
- Wong, W., Aloyz, J., Ballabriga, R., Campbell, M., Kremastiotis, I., Llopart, X., Poikela, T., Sriskaran, V., Tlustos, L., Turecek, D., 2020. Introducing Timepix2, a frame-based pixel detector readout ASIC measuring energy deposition and arrival time. *Radiat. Meas.* 131, 106230.
- Yamamoto, T., 2011. RPL dosimetry: Principles and applications. In: *AIP Conference Proceedings*. American Institute of Physics, pp. 217–230.
- Yasuda, H., Fujitaka, K., 2000. Responses of TLD $\text{Mg}_2\text{SiO}_4:\text{Tb}$ and radiophotoluminescent glass to heavy charged particles and space radiation. *Radiat. Prot. Dosim.* 87, 115–119. <http://dx.doi.org/10.1093/oxfordjournals.rpd.a032983>.
- Yasuda, H., Fujitaka, K., 2002. Efficiency of a radiophotoluminescence glass dosimeter for low-earth-orbit space radiation. *Radiat. Prot. Dosim.* 100, 545–548.
- Yasui, K., Omachi, C., Nagata, J., Toshito, T., Shimizu, H., Aoyama, T., Hayashi, N., 2021. Dosimetric response of a glass dosimeter in proton beams: LET-dependence and correction factor. *Phys. Medica* 81, 147–154.
- Young, D.A., 1958. Etching of radiation damage in lithium fluoride. *Nature* 182, 375–377.
- Yukihiro, E.G., Christensen, J.B., Togno, M., 2022a. Demonstration of an optically stimulated luminescence (OSL) material with reduced quenching for proton therapy dosimetry: $\text{MgB}_4\text{O}_7:\text{Ce,Li}$. *Radiat. Meas.* 152, 106721.
- Yukihiro, E.G., Doull, B.A., Ahmed, M., Brons, S., Tessonnier, T., Jäkel, O., Greilich, S., 2015. Time-resolved optically stimulated luminescence of $\text{Al}_2\text{O}_3:\text{C}$ for ion beam therapy dosimetry. *Phys. Med. Biol.* 60, 6613–6638.
- Yukihiro, E.G., McKeever, S.W.S., 2006. Spectroscopy and optically stimulated luminescence of $\text{Al}_2\text{O}_3:\text{C}$ using time-resolved measurements. *J. Appl. Phys.* 100, 083512.
- Yukihiro, E.G., McKeever, S.W.S., Andersen, C.E., Bos, A.J.J., Bailiff, I.K., Yoshimura, E.M., Sawakuchi, G.O., Bossin, L., Christensen, J.B., 2022b. Luminescence dosimetry. *Nature Rev. Methods Prim.* 2.
- Yukihiro, E.G., Sawakuchi, G.O., Guduru, S., McKeever, S.W.S., Gaza, R., Benton, E.R., Yasuda, N., Uchihori, Y., Kitamura, H., 2006. Application of the optically stimulated luminescence (OSL) technique in space dosimetry. *Radiat. Meas.* 41, 1126–1135.
- Yukihiro, E.G., Yoshimura, E.M., Lindstrom, T.D., Ahmad, S., Taylor, K.K., Mardirossian, G., 2005. High-precision dosimetry for radiotherapy using the optically stimulated luminescence technique and thin $\text{Al}_2\text{O}_3:\text{C}$ dosimeters. *Phys. Med. Biol.* 50, 5619–5628.
- Zirkle, R.E., Marchbank, D.F., Kuck, K.D., 1951. Exponential and Sigmoid Survival Curves Resulting from Alpha and X Irradiation of *Aspergillus* Spores. Report, Institute of Radiobiology and Biophysics, University of Chicago, Argonne National Laboratory.